

Computational Modeling of Human Head Model for Correlation
Study of Cerebrospinal Fluid and Tumor



Author

Muhammad Uzair Ul Haq

Regn Number

00000206567

Supervisor

Dr. Zartasha Mustansar

**SCHOOL OF MECHANICAL & MANUFACTURING ENGINEERING
NATIONAL UNIVERSITY OF SCIENCES AND TECHNOLOGY,
ISLAMABAD
September 2020**

**Computational Modeling of Human Head Model for Correlation
Study of Cerebrospinal Fluid and Tumor**

Author

Muhammad Uzair Ul Haq

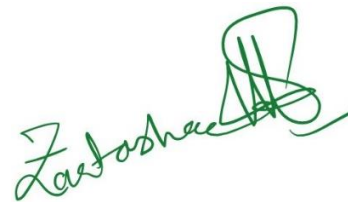
Regn Number

00000206567

**A thesis submitted in partial fulfillment of the requirements for the degree of
MS Biomedical Engineering**

Thesis Supervisor:

Dr. Zartasha Mustansar



Thesis Supervisor's Signature

**SCHOOL OF MECHANICAL & MANUFACTURING ENGINEERING
NATIONAL UNIVERSITY OF SCIENCES AND TECHNOLOGY,
ISLAMABAD
September 2020**

Declaration

I certify that this research work titled “*Computational Modeling of Human Head Model for Correlation Study of Cerebrospinal Fluid and Tumor*” is my own work. The work has not been presented elsewhere for assessment. The material that has been used from other sources it has been properly acknowledged / referred. I have extensively used some of the material from my research on this topic wherever need be, in the best interest, to do justice with this thesis and therefore I have duly cited and acknowledged that with great care. The thesis is submitted with signature of the supervisor and mine and has been proof-read for errors.

Signature of Student

Muhammad Uzair Ul Haq

00000206567

Plagiarism Certificate (Turnitin Report)

This thesis has been checked for Plagiarism. Turnitin report endorsed by Supervisor is attached.

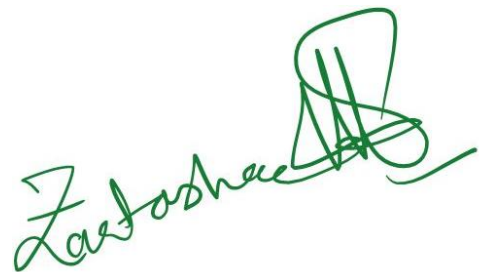
Signature of Student

MUHAMMAD UZAIR UL HAQ

Registration Number: 00000206567

Name & Signature of Supervisor

DR. ZARTASHA MUSTANSAR

A handwritten signature in green ink, appearing to read 'Zartasha Mustansar', with a stylized flourish at the end.

Signature: _____

Copyright Statement

- Copyright in text of this thesis rests with the student author. Copies (by any process) either in full, or of extracts, may be made only in accordance with instructions given by the author and lodged in the Library of NUST School of Mechanical & Manufacturing Engineering (SMME). Details may be obtained by the Librarian. This page must form part of any such copies made. Further copies (by any process) may not be made without the permission (in writing) of the author.
- The ownership of any intellectual property rights which may be described in this thesis is vested in NUST School of Mechanical & Manufacturing Engineering, subject to any prior agreement to the contrary, and may not be made available for use by third parties without the written permission of the SMME, which will prescribe the terms and conditions of any such agreement.
- Further information on the conditions under which disclosures and exploitation may take place is available from the Library of NUST School of Mechanical & Manufacturing Engineering, Islamabad.

I Dedicate this thesis to my exceptional parents whose tremendous support and cooperation led me to this wonderful accomplishment.

Abstract

Cerebrospinal fluid (CSF) plays a pivotal role in regulating homeostasis and maintaining intracranial pressures (ICP) in human brain. Under histological condition such as brain tumor, CSF flow can be disturbed resulting in increase or decrease in ICP. Current common techniques available to monitor ICP requires an invasive procedure, where a catheter is inserted into human brain to study CSF flow and ICP. However, in the recent decade, focus is shifting from invasive procedures to non-invasive techniques using computational modeling. Current research aims to develop a computational model to study the effect of brain tumor growth on the flow on CSF in human brain. Proposed method invokes the use of Fluid-structure interaction (FSI) to consider for the tumor-ventricular wall interaction on CSF flow. Simulation is carried for two cases. One scenario, models the normal case wherein no tumor is present in the patient, while second scenario considers the tumor specific patient. Results obtained shows that there is considerable change in flow parameters for a tumor patient. A mean rise of 74.23% in CSF velocity indicates that flow profile is largely affected due to external forces of tumor. Findings suggest that taking deformable character of ventricular walls is a necessary parameter in modeling CSF flow mechanics in the brain ventricles. Furthermore, we also conclude that compressive forces of brain tumor on ventricular walls can significantly influence the outcome of CSF flow in cranium and must be addressed in patients in clinical care.

Key Words: *Intracranial pressure (ICP), Cerebrospinal Fluid (CSF), Finite Element method, Image based Modeling, Fluid-Solid Interaction, Non-invasive treatment*

Table of Contents

Declaration	iii
Plagiarism Certificate (Turnitin Report)	iv
Copyright Statement	v
Abstract	vii
Table of Contents	viii
List of Abbreviations	x
List of Figures	xi
List of Tables	xii
CHAPTER 1: INTRODUCTION	1
1.1 Introduction	1
1.2 Motivation	2
1.3 Research Questions and Scope.....	3
1.4 Deliverables and Objectives.....	3
1.5 Summary	5
CHAPTER 2: LITERATURE REVIEW	6
2.1 Summary	12
CHAPTER 3: THEORY	13
3.1 Fluid–Structure Interaction	13
3.2 System of Equations.....	13
3.3 FSI Coupling Methods	15
3.3.1 Monolithic Coupling.....	15
3.3.2 Weak Coupling	16
3.3.3 Strong Coupling.....	16
3.4 FSI Data Transfer Methods	17
3.4.1 One-Way FSI	17
3.4.2 Two-Way FSI.....	18
3.5 Summary	20
CHAPTER 4: METHODOLOGY	21
4.1 Data Acquisition.....	21
4.2 Segmentation.....	21
4.3 Geometry and 3D-Reconstruction.....	23

4.4	Meshing	23
4.4.1	Structural Mesh.....	24
4.4.2	Fluid Mesh	25
4.5	Boundary Conditions.....	26
4.6	Tumor Growth Model	28
4.7	Numerical Simulation	30
4.7.1	CFD Analysis Setup.....	30
4.7.2	Dynamic Meshing.....	32
4.7.3	Structural Mechanics Setup	32
4.7.4	FSI Coupling Mechanism	33
4.7.5	Time-Step Size and Convergence Criterion	33
4.8	Summary	35
CHAPTER 5: RESULTS AND DISCUSSION		36
5.1	Model Validation.....	36
5.2	CSF Flow Properties	36
5.3	CSF Flow Field Pulsatility	38
5.4	Flow Parameterization under Cardiac cycle.....	38
5.5	Reverse Flow in Fourth Ventricle during Cardiac Systole-Diastole.....	39
5.6	Pressure Field	40
5.7	Total Deformation of Ventricles	41
5.8	Comparison of Results	42
5.9	Statistical Analysis	44
5.9.1	CSF Velocity Correlation with Tumor	45
5.9.2	Deformation Correlation with Tumor.....	46
CHAPTER 6: CONCLUSION AND CONTRIBUTIONS.....		47
6.1	Conclusion.....	47
6.2	Research Contributions	48
CHAPTER 7: LIMITATIONS AND FUTURE WORK.....		50
REFERENCES.....		52

List of Abbreviations

ICP	Intracranial Pressure
MAP	Mean Arterial Pressure
CPP	Cerebral Perfusion Pressure
TBI	Traumatic Brain Injury
MRI	Magnetic Resonance Imaging
WM	White Matter
GM	Gray Matter
CNS	Central Nervous System
PNS	Peripheral Nervous System
SNS	Somatic Nervous System
ANS	Autonomic Nervous System
ENS	Enteric Nervous System
CSF	Cerebrospinal Fluid
GCS	Glasgow Comma Scale
EVD	External Ventricular Drainage
TCD	Transcranial Doppler Ultrasonography
FEM	Finite Element Method
FSI	Fluid Structure Interaction
ROI	Region of Interest
HGG	High Grade Gliomas
LGG	Low Grade Glioma
ALE	Arbitrary Lagrangian Eulerian
PISO	Pressure Implicit with Splitting of Operators
ILU	Incomplete Lower Upper
AMG	Algebraic Multigrid Method
CFL	Courant-Friedrichs-Lewy number

List of Figures

Figure 1 Simplified geometry of cerebral aqueduct [14].....	6
Figure 2 3D representation of the models, (a) Cylindrical model (b) Anatomical model obtained from MRI scans [15]	7
Figure 3 Three-dimensional representation of intra-cerebral CSF [15].....	7
Figure 4 Simplified ventricular geometry [16]	8
Figure 5 Segmented and labelled ventricles from MRI scans [19].....	9
Figure 6 Velocity contours (mm/s) taken from a plane through the VS at the time in the cycle of maximum velocity. [19].....	9
Figure 7 2D-Model of brain (a) brain tissue with FEM mesh (b) displacement of brain tissues [20].....	10
Figure 8 Monolithic coupling approach.....	15
Figure 9 Weak coupling approach	16
Figure 10 Strong coupling approach.....	17
Figure 11 One-way data transfer (a) Data transfer from Solid to Fluid domain, (b) Data transfer from Fluid to Solid domain.....	18
Figure 12 Two-way data transfer	19
Figure 13 Raw MRI slice (a) Sagittal section of MRI scan of human brain, b) Axial section of MRI scan of human brain	21
Figure 14 (a) T1-contrast enhanced axial scan; (b) Ventricles segmented from T1-contrast enhanced axial scan.....	22
Figure 15 Representation of ventricles; (a) shows Axial section of MRI image of human brain showing ventricles and tumor; (b) shows highlighted ROI of ventricles; (b) and (c) show 3D reconstructed ventricular geometry in lateral and isometric view	23
Figure 16 Shape representation of a shell element ¹	24
Figure 17 Mesh convergences of structural domain	25
Figure 18 Finite element model mesh.....	25
Figure 19 Mesh convergence of fluid domain	26
Figure 20 Boundary condition diagram	27
Figure 21 Predicted tumor growth (a) volume (b) force.....	29
Figure 22 Velocity vector plots in third and fourth Ventricle; (a) represents the case of no tumor, and (b) represents the case with tumor	36
Figure 23 Pulsatile mass flowrate at inlets; Peak pressures in the lateral ventricles, and CSF velocity in cerebral aqueduct.	39
Figure 24 Visualization of velocity vectors in fourth ventricle at various timesteps. Case A represents velocity vectors in fourth ventricles for without tumor; and Case B represents velocity vectors in fourth ventricles for tumor.	40
Figure 25 Pressure on ventricle wall. (a) shows pressures without tumor; and (b) shows pressure under tumor forces	41
Figure 26 Deformation of ventricle wall. (a) shows deformation without tumor; and (b) shows deformation under tumor forces.....	42
Figure 27 ANOVA analysis, CSF Velocity vs Tumor.....	45
Figure 28 ANOVA analysis, Deformation vs Tumor	46

List of Tables

Table I Ventricular and Tumor Volume Validation Against Ground Truths	22
Table II Boundary Conditions	28
Table III Calculated Tumor Volume and Force	30
Table IV Calculated Tumor Volume and Force.....	37
Table V Deformation comparison with and without the influence of tumor	41
Table VI Comparison of results obtained from the proposed method against previous studies..	43
Table VII Patient data for statistical study.....	44

CHAPTER 1: INTRODUCTION

1.1 Introduction

The human brain is the most sensitive organ of the body. Entire functioning of body depends upon adequate sensory and motor response from brain in the form of neuronal signals [1]. It is shelled by skull which is rigid in nature. It protects brain from any external injury [2]. It also preserves the intracranial environment which is quite sensitive and susceptible to external influences. Whereas, inside the cranium Cerebrospinal fluid (CSF) provides the same protection for any internal frictional or intravenous interventions. It provides buoyancy which effectively reduces the weight of brain [3].

The intracranial environment can be affected by changes of the CSF flow inside the human ventricular system (HVS) if its pathway is blocked [4]. Hence, if CSF flow is obstructed the pressures generated thereof would consequently disturb and destabilize the intracranial homeostasis [4-8]. This thesis, in its fundamentals, would attempt to find an answer as to how the entire CSF mechanics is generally influenced by external factors. The external factor which is distinguished in this study is that it considers the role and biomechanical effects of brain tumor as such. This study attempts to unearth the overall biomechanics of CSF-tumor interaction and how *inter-se* relationship causes CSF pressures and velocity to rise, sometimes exponentially. Furthermore, while considering the role of brain tumor on the walls of ventricles, a generic method is provided using Fluid-Structure Interaction (FSI) scheme whereby both fluid and solid interactions are modeled. To quantify the effects of brain tumor on CSF flow velocity, a statistical study is carried among 14 subjects whereby interaction of tumor forces with CSF flow is calculated and a qualitative relationship, if any, is presented. Analysis of Variance (ANOVA) is used to find such relationship, if any. In addition, the aim of this thesis is also present a model whereby some other pathological effects can be studied such as edema, hematoma, obstructive hydrocephalus, communicating hydrocephalus *et cetera*. In modeling supra effects, some reasonable assumptions have to be made, in conjunction with the modeled presented herein, to model such pathologies as well.

The method presented herein can also be used in cases relating to intracranial pressure (ICP) mechanics because, among other factors, CSF flow pressures are pivotal in cases of elevated

ICP. Hence, the model presented in this thesis, if applied objectively, can also be used in clinical scenarios and conditions pertaining to ICP biomechanics such as in traumatic brain injury cases etc.

1.2 Motivation

According to a survey conducted by Central Brain Tumor Registry of the United States (CBTRUS) [9], around 700,000 Americans are currently living with brain tumor. Furthermore 69.8 % are benign whereas 30.2 % are malignant. The survival rate for malignant brain tumor patients is only 36 %. Therefore, if brain tumor is detected in early stage then the chances of patient's survival significantly increases. According to another survey published by [10], Brain tumor is the 10th leading cause of death for men and women. It is estimated that 18,020 adults will die from primary brain tumors this year. The 5-year survival rate for people with brain tumor is around 36%. The recent surveys have raised the alarming situation. Based on the recent surveys the early diagnosis of tumor and study the brain dynamics has become a primary task for researchers [11].

Most of the techniques which are used to diagnose and study brain dynamics requires an intensive invasive procedure which requires a catheter to be inserted in to human brain [12]. The invasive procedures are critical as they require surgical expertise. Furthermore, performing brain tumor surgery without any prior information also poses a risky situation for surgeons and clinicians.

The proposed research introduces a non-invasive technique to detect and study the brain tumor in early stages. Brain tumor has a significant influence on the neurological state of a person. If tumor has reached metastasis stage, it can aggressively spread to different parts of body and also quite significantly damage the surrounding brain tissue thereby inducing deadly neuropathological consequences, inter-alia, ischemia, herniation, stroke et cetera [6]. This study will equip clinicians and surgeons with the knowledge to better diagnose the brain infections such as brain tumor and will also help them to study different brain pathologies such as edema, hematoma, obstructive hydrocephalus, communicating hydrocephalus etc. As the previous techniques are subjective to human error, the proposed research is an automated technique which removes the subjectivity from

measurement and analysis. Proposed research will be mainly focused on studying the relative effects of brain tumor on the walls of ventricles and how CSF flow is disturbed.

1.3 Research Questions and Scope

In recent decade, numerical methods along with computer simulations are commonly being used to discretize real life scenarios such as blood flow in arteries, cardiac muscle modeling et cetera [14-21]. In research areas containing biomedical applications such techniques are useful because they are non-invasive [13] and allow clinicians to take informed decisions prior to any sensitive invasive procedure. Computational fluid dynamics (CFD) has been widely used to model CSF flow. Analysis of CSF behavior and properties such as velocity profile and pressure drop through ventricles under influence of any pathology allow the clinicians to differentiate between normal and abnormal cases.

In the past research, the assumptions regarding the Human Ventricular System (HVS) are over simplified [14] which in some cases contradicts with the real brain anatomy. The results obtained from these studies limits their applicability to be used in real life. The ventricular body is considered as rigid by many researchers [19], whereas the brain ventricles are deformable in nature [1]. Likewise, the flow of cerebrospinal fluid (CSF) is also simplified to a simple flow whereas in nature [14], the CSF flow is pulsatile and it is heavily induced by cardiac pulsations.

The proposed research addresses all the short comings which were present in the previous studies. The HVS is segmented from a tumor specific patient. The ventricular walls are modeled as deformable to better study the effect of brain tumor and the flow of CSF. The cardiac pulsations are also incorporated to study the effect of systole and diastole on CSF flow in normal and abnormal cases.

1.4 Deliverables and Objectives

The deliverables of the proposed research are as follows.

1. Accurate segmentation of brain ventricles and Tumor
2. 3D-reconstruction of human head model. Fine tuning of model for anomalies detection.
The constructed 3D-model will then be used in Finite Element Method analyzed.
3. Analyzing the behavior of CSF in brain mechanics.

4. Developing Fluid Structure interaction (FSI) between both structural and fluid parts.
5. Finding correlation of CSF under the influence of tumor

1.5. Summary

This chapter describes that

- Brain tumor is one of the severe brain pathology, the survival rate for which is only 36 % if not detected in early stage.
- Invasive procedures are critical and human subjective therefore, the solution lies in non-invasive techniques.
- Computational modeling provides a promising solution to solve biomedical problems.
- Previous studies have used the over simplified assumptions which limits their use in real life.
- Proposed research addresses all the short comings present in the past researches and studies.

CHAPTER 2: LITERATURE REVIEW

In recent decade, numerical methods along with computer simulations are commonly being used to discretize real life scenarios such as blood flow in arteries, cardiac muscle modeling et cetera. In research areas containing biomedical applications such techniques are useful because they are non-invasive and allow clinicians to take informed decisions prior to any sensitive invasive procedure. Computational fluid dynamics (CFD) [22] has been widely used to model CSF flow. Analysis of CSF behavior and properties such as velocity profile and pressure drop through ventricles under influence of any pathology allow the clinicians to differentiate between normal and abnormal cases.

CSF modeling has been of great interest by researchers from across the globe. For instance, E. E. Jacobson et al. [14] proposed a simple cylinder model to study the flow of CSF through of cerebral aqueduct. Their study suggests that pressure difference of atleast 1.1 Pa is required to drive the CSF from cerebral aqueduct. The geometry proposed in their work is shown in Figure 1.

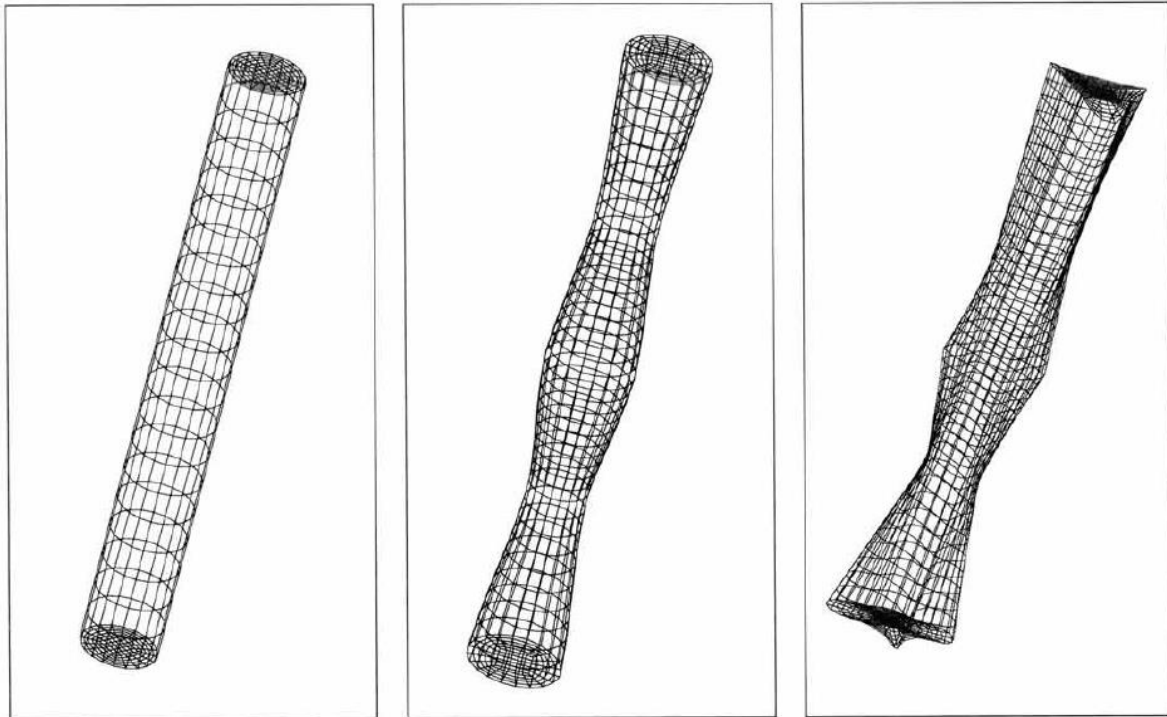


Figure 1 Simplified geometry of cerebral aqueduct [14]

L. Fin and R. Grebe [15] also proposed two models shown in Figure 2, cylindrical rigid wall model and elastic wall model segmented from MRI data to study the flow of CSF in Aqueduct of Sylvius (AS) as shown in Figure 3. The spatial domain was digitized using Immersed Boundary method (IBM) [9]. Pulsatile inlet velocity boundary condition is used, and their results show pressure drop of 1.02 Pa and velocity of 30.20 mm/s for cylindrical model; whereas for elastic wall model, the pressure drop of 2.91 Pa and velocity of 64.65 mm/s was recorded.

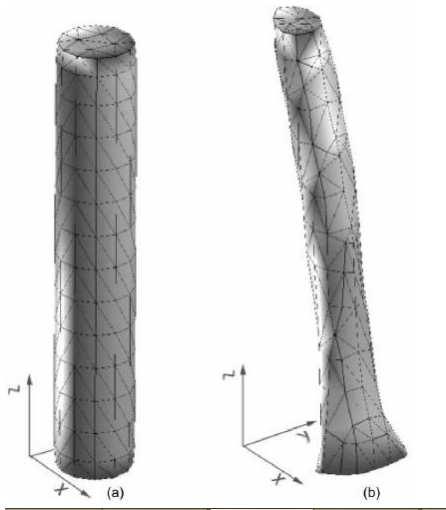


Figure 2 3D representation of the models, (a) Cylindrical model (b) Anatomical model obtained from MRI scans [15]

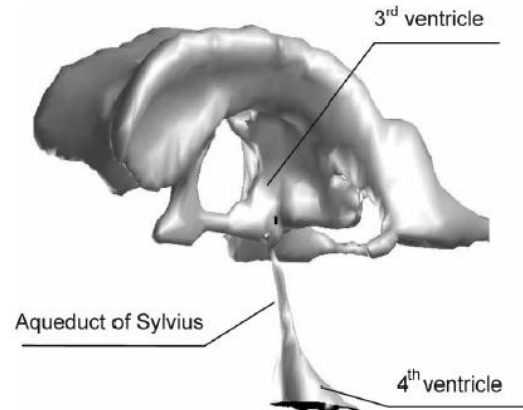


Figure 3 Three-dimensional representation of intra-cerebral CSF [15]

In another case study, A. A. Linninger et al [16] proposed a 2D rigid model of HVS where the pressure drop of less than 2 Pa and velocity of 7.3 mm/s is reported. V. Kurtcuoglu et al. [17] constructed a simplified geometry of HVS to model the mechanical behavior of CSF. Figure 4 shows the simplified geometry proposed by [17]. To drive the flow of CSF, oscillating wall of third ventricle was used whereas at outlet zero pressure boundary condition was applied. They deduced that pressure increases in lateral ventricles due to aqueduct stenosis but no significant phase difference between wall motion and pressure was observed.

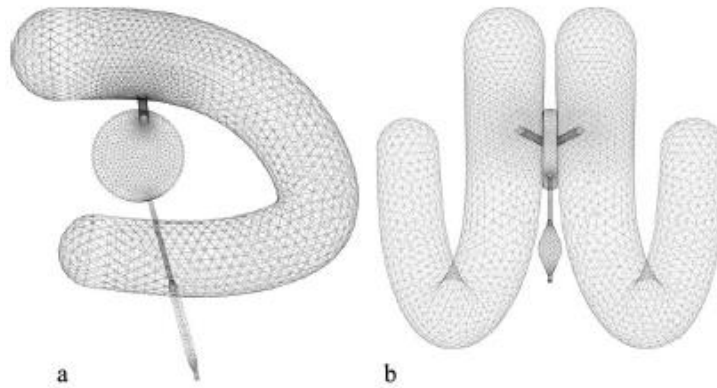


Figure 4 Simplified ventricular geometry [16]

On the nature of flow field of CSF, E. E. Jacobson et al. [18] has reported the flow profile of CSF to be pulsatile in nature. Moreover, the CSF movement is influenced by the pathway of CSF through CNS and brain movement. In addition, the pulsatile nature of CSF is also due to the elastic nature of the Ventricular space, and due to the changes in systolic and diastolic pressure in each cardiac cycle [23-24]. The CSF pulsatile flow and the associated pulsatile wave nature was first reported by Portnoy & Chopp [24] to be the combination of sinusoidal waves. One of the extensive and supportive studies on simple CSF flow in the HVS is documented by L. Howden et al. [19]. 3D Ventricles shown in Figure 5 were segmented from MRI data with 1 mm voxel size using MIMICS. A commercial code of Fluent was used for CFD analysis. CSF is treated as incompressible Newtonian fluid. Pulsatile velocity inlet and zero-gauge pressure at outlet boundary conditions were used. The maximum velocity and Reynolds number was found to be 11.38 mm/s and 15 in cerebral aqueduct respectively [19]. However, in this study the walls of ventricles are taken as rigid and effects of Fluid-structure interaction are neglected. Figure 6 shows the velocity contours through different regions of brain ventricles.

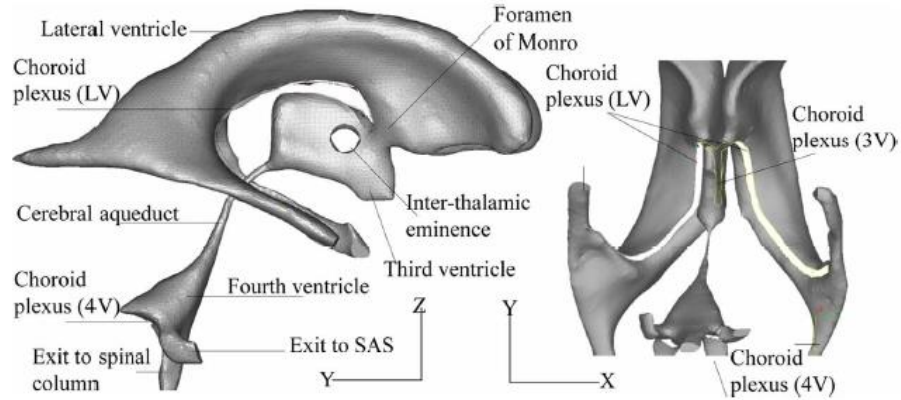


Figure 5 Segmented and labelled ventricles from MRI scans [19]

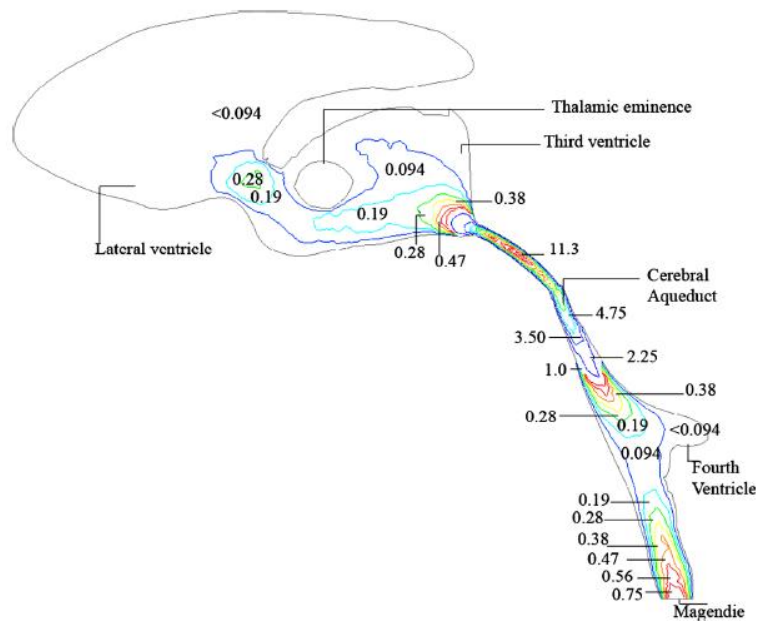


Figure 6 Velocity contours (mm/s) taken from a plane through the VS at the time in the cycle of maximum velocity. [19]

In past, CSF modeling has been limited to a simple flow analysis—by taking ventricular walls as rigid, ignoring completely the influence of deformable nature of ventricles, thus hindering in reaching towards a complete understanding of flow dynamics and tissue interaction mechanics. Another reason why this approach of modeling is problematic is due to the fact that by considering the walls as rigid, effect of the external forces such as that of brain tumor cannot be included into broader framework of how tumor effects the CSF flow parameters within the brain ventricles.

Thus, a course correction in approach for modeling such situations is needed. Fluid-Structure interaction (FSI) is one area which has been widely used in areas concerning inter se interactions in various Multiphysics problems, such as modeling the effect of tumor on the CSF flow profile and the resistance of the flow on the ventricle tissue mechanics.

With regards to taking ventricular walls as deformable, much of the work is restricted to 2D modeling; and one of the studies related to present discussion is documented by N. Masoumi et al [21]. The authors have proposed a 2D computational model of CSF flow from human ventricular system using FSI. 2D geometry was constructed using MRI images from 1.5 Tesla machine. FSI simulation was performed in ADINA software. CSF is treated as incompressible fluid. Pulsatile velocity inlet, based on cardiac heart cycle, and zero pressure at outlet boundary conditions are used. The authors have performed simulations on two models: 1) taking ventricle wall as flexible; and 2) taking wall as Rigid. The flexible wall model produced better results compared to rigid wall model as it could mimic the diastolic backflow. The maximum velocity in cerebral aqueduct for rigid and flexible model is found to be 11 mm/s and 8 mm/s respectively. The total pressure drop for rigid and flexible model is reported to be 3.5 Pa and -0.2 to 2.4 Pa respectively. Maximum displacement reported by the authors for the walls of ventricles is 0.006 mm. However, this study is limited owing to the approximation of assuming it as a 2D case. By modeling ventricular body in 2D, most non-linear interactions are missed out which are otherwise present in a full spectrum 3D modeling.

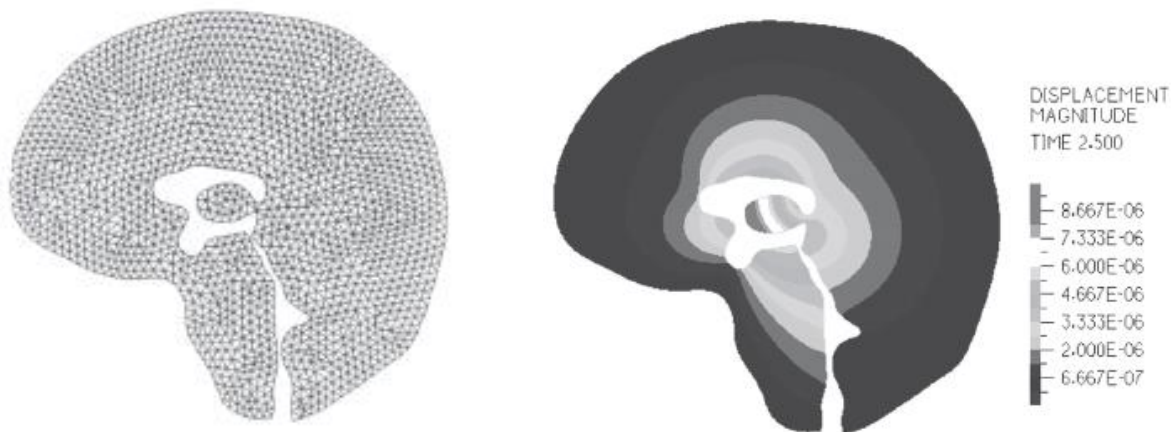


Figure 7 2D-Model of brain (a) brain tissue with FEM mesh (b) displacement of brain tissues [20]

In view of what has been discussed above, a unified study is needed which takes into consideration the entire 3D ventricular body as deformable and records the effects of solid flexible walls on CSF fluid profile and vice versa. The proposed study is a step towards modeling CSF flow in ventricles using FSI. In particular, it aims to address the question of how brain tumor can affect the CSF flow in the ventricles.

2.1 Summary

This chapter describes that

- In the past research ventricular geometry was overly simplified which contradicts with the real brain anatomy
- 3D-models produce superior results and gives better understanding of intra brain fluid dynamics and structural interaction.
- Deformable ventricular models produce better results than rigid models.
- Fluid-Structure Interaction (FSI) techniques are only used for 2D-anaylsis. However, a 3D-FSI approach will help better understand the brain dynamics and interaction with surrounding tissues compared with the past approaches.

CHAPTER 3: THEORY

This chapter discusses the complete theory of Fluid-Structure Interaction (FSI) technique. System of equations, methods of FSI modeling, coupling methods and data transfer methods.

3.1 Fluid–Structure Interaction

21st century has seen a paradigm shift as the focus is increasing towards solving Multiphysics problem. In the past, solid mechanics, fluid mechanics and heat transfer systems were modeled separately [29]. The individual response of these models handicaps the researchers to study the interaction of different physical domains.

Fluid–Structure Interaction (FSI) modeling is a computational modeling technique which involves the interaction of multiple physical phenomena such as solid, fluid, heat transfer and electromagnetism etc [30]. In FSI different physical domains are simulated simultaneously to obtain single result, that cannot be produced if each physical phenomenon was modeled individually [30]. In Biomedical domain, FSI modeling is commonly used to model blood flow in arteries, fluid dynamics in human brain, cardiac muscle modeling et cetera [25-27]. Examples of systems that require FSI modeling are the, blood flow in arteries, motion of heart valves, fluid dynamics of brain and tissue interaction and thin structures of human body.

These examples require the Computational Fluid Dynamics (CFD) and Finite Element Analysis (FEA) models be linked together so that the results of each model impart forces on the other. Traditionally, the phenomena of fluid dynamics and solid mechanics have been evaluated separately [31]. However, with advent of supercomputers, increased computational resources, commercially available software, and new techniques to add computational stabilities, it has become a feasible task to apply computational techniques to solve multiphysics problems [28].

3.2 System of Equations

The computational model containing the fluid domain utilizes the three-dimensional Navier–Stokes equations (NSE) in conjunction with the continuity, volume fraction, and energy equations as shown in equation 1 and 2. In this study, Fluent module is used to solve Navier–Stokes equations using the pressure-based solver. In the pressure-based solver, the momentum and continuity

equations, are used in combination to calculate the pressure field, and the mass balance equation must be evaluated to conserve the overall mass of the system.

$$\nabla \cdot (\rho \cdot \vec{v}) = 0 \quad (1)$$

$$\rho \frac{\partial \vec{v}}{\partial t} + \rho(\vec{v} \cdot \nabla)\vec{v} = -\nabla P + \tau\rho + \mu\nabla^2\vec{v} \quad (2)$$

where ρ is the density of fluid, v is the velocity of the fluid, ∇ is the gradient operator, $\rho \frac{\partial \vec{v}}{\partial t}$ is the local acceleration of fluid particles, $\rho(\vec{v} \cdot \nabla)\vec{v}$ is the convective acceleration, ∇P is the pressure gradient, $\tau\rho$ are body forces, $\mu\nabla^2\vec{v}$ is the viscous term which resists the motion of the fluid particles.

The computational model containing the solid mechanics utilized the three-dimensional strain displacement, nodal displacement, and stress equations, Equations 3 through 5 respectively, to solve for the deformation, stress, strain, and forces across each node in the solid domain.

$$[B] = [\partial][N] \quad (3)$$

$$\{\varepsilon\} = [B]\{D\} \quad (4)$$

$$\{\sigma\} = [E]\{\varepsilon\} \quad (5)$$

Where B is the strain displacement, ∂ is the four-dimensional gradient (time and space), N is element shape function, ε is strain, D is nodal displacements, σ is stress, and E is modulus of elasticity.

3.3 FSI Coupling Methods

FSI modeling involves the linking of solid mechanics and fluid mechanics together. Combined effect of these phenomenon models the real-life scenario in a more realistic way compared to if these phenomena were modeled separately. FSI modeling allow the transfer of data in terms of forces and displacements between solid and fluid domain [29]. Based on how the data is transferred between different modules such as FEA and CFD, the FSI modeling is categorized in three main approaches.

3.3.1 Monolithic Coupling

In monolithic coupling the systems of equations are solved simultaneously as shown in Figure 8. Both solid and fluid equations are lumped into a single equation matrix. Usually monolithic coupling requires custom coding for each specific problem and they also computationally expensive.

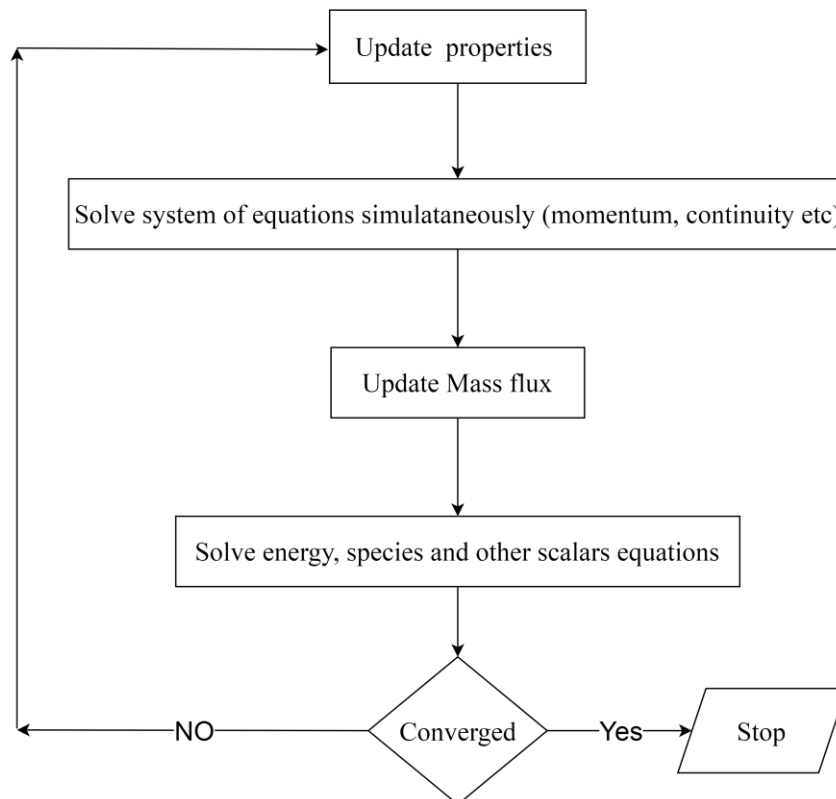


Figure 8 Monolithic coupling approach

3.3.2 Weak Coupling

Weak coupling is a type of partitioned approach unlike monolithic coupling. In weak coupling the data between solid and fluid domains are exchanged once every time-step. Additionally, the convergence criteria are not checked at each time step which may result an erroneous data being exchanged between solid and fluid domain resulting an inaccurate result. The weak coupling work flow is shown in Figure 9.

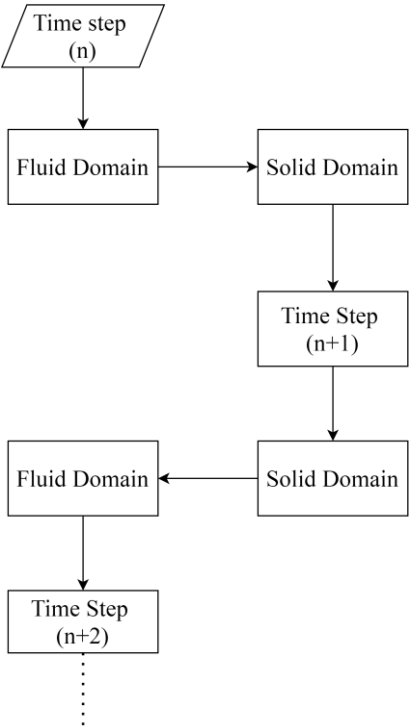


Figure 9 Weak coupling approach

3.3.3 Strong Coupling

In strong coupling, the result of each domain is calculated once and then the data is exchanged between the solid and fluid domains as shown in Figure 10. The boundary conditions are then updated for the same time step for reevaluation of the results. The process of data exchange is repeated until the convergence criteria is achieved.

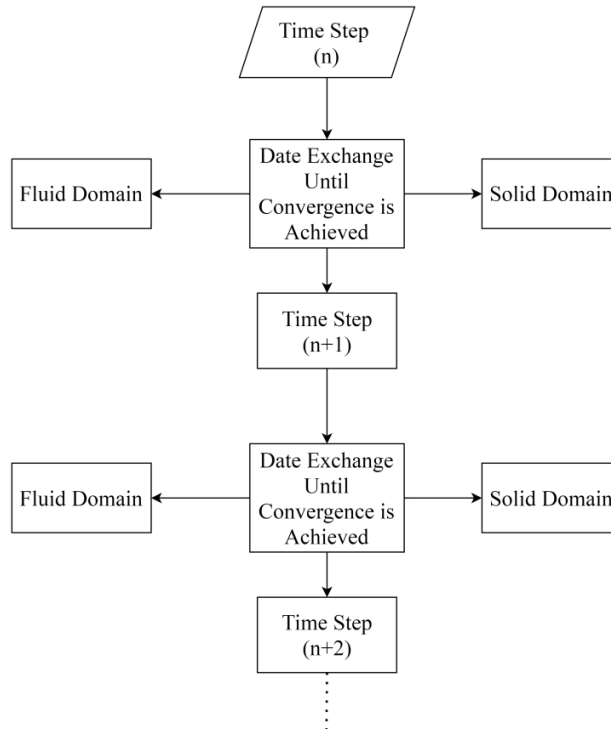


Figure 10 Strong coupling approach

3.4 FSI Data Transfer Methods

FSI simulations involves the data transfer between multiple domains to solve multiphysics problem. The data transfer between domain can be one-way or two-way depending upon the application and the phenomenon to model.

3.4.1 One-Way FSI

In one-way FSI the data is transferred only from one domain to the other i-e the data can be transferred from either solid to fluid domain or from fluid to solid domain. The simultaneous exchange of data cannot take place in one-way FSI. One-way FSI is computationally less expensive compared to two-way FSI. The one-way FSI is useful when the result of one domain has negligible effect on the other domain. Example of one-way FSI includes the effect of air stream on building`s window in this scenario the air steam can have effect on the window of building and it can deform it in case of tornado but the deformation of window will have insignificant effect on the air present around it. The one-way scheme is shown in Figure 11.

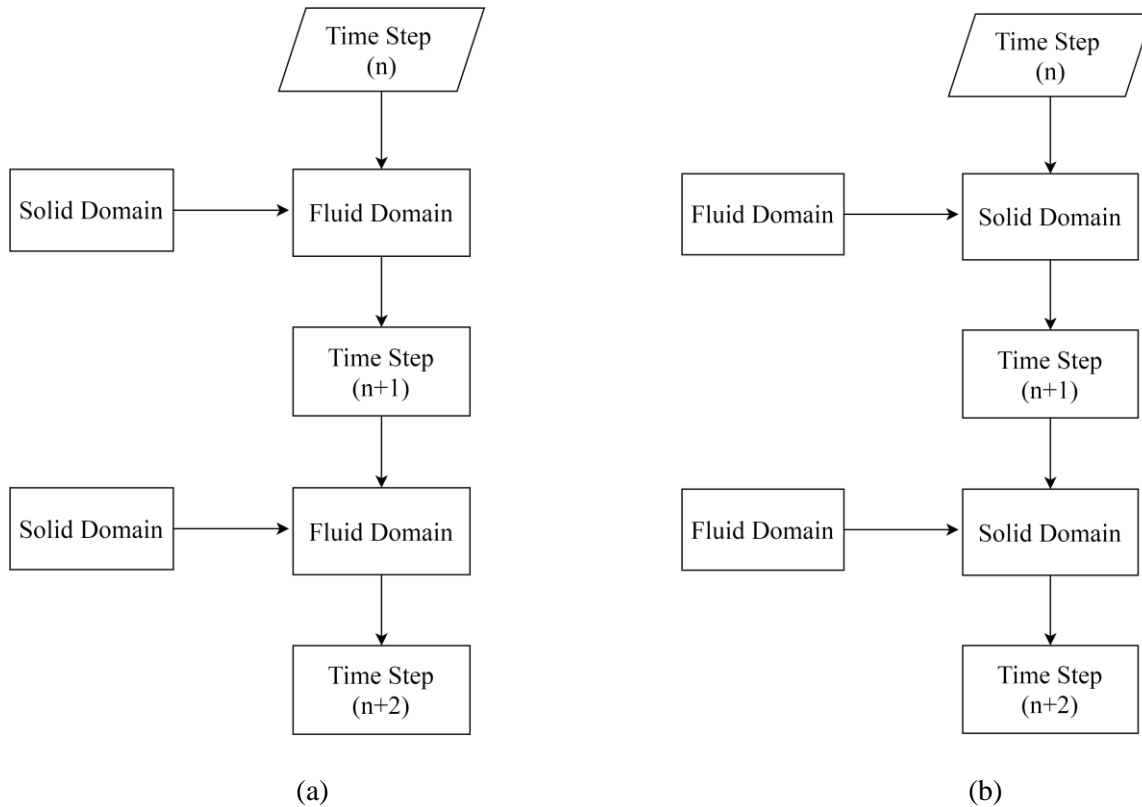


Figure 11 One-way data transfer (a) Data transfer from Solid to Fluid domain, (b) Data transfer from Fluid to Solid domain

3.4.2 Two-Way FSI

In two-way FSI data is simultaneously transferred between solid and fluid domains. The data is exchanged between both the domains at each time step and result is evaluated for convergence. It is computationally more expensive than one-way FSI. Two-way data transfer is more powerful and versatile. This type of data transfer is used to model phenomenon which involves large deformations. This technique is usually used in biomedical applications such as blood flow in artery, cardio vascular movement, cerebrospinal fluid modeling etc. In term of modeling the disadvantage of two-way FSI includes instabilities and convergence problems which ultimately leads to solver divergence. The data transfer of two-way FSI is shown in Figure 12.

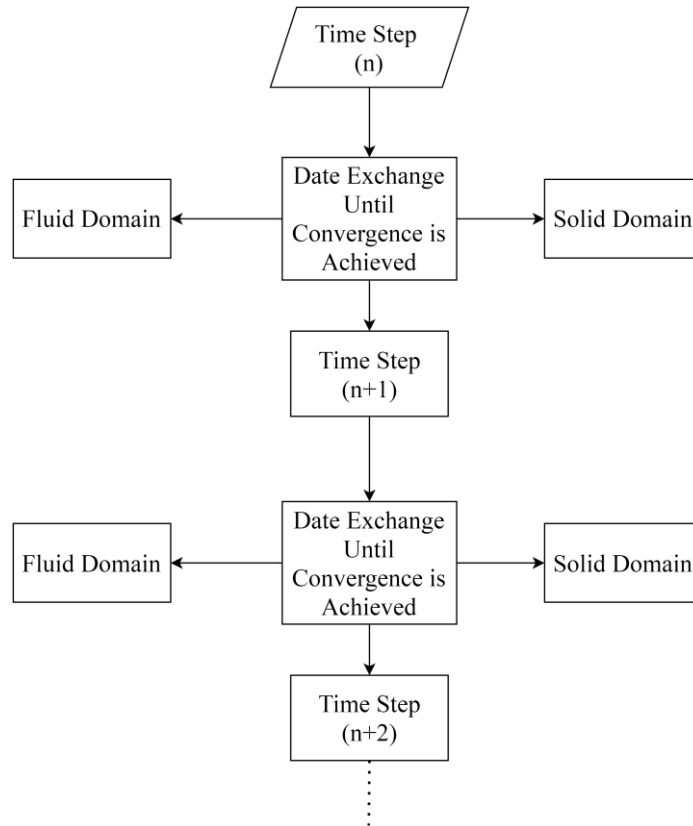


Figure 12 Two-way data transfer

3.5 Summary

This chapter describes that

- Conventional CFD and FEA modeling techniques have limitations due to which they cannot solve Multiphysics problems.
- Fluid-Structure Interaction is a promising technique for solving multi domain problems.
- FSI simulations require coupling of solid mechanics and fluid mechanics.
- Different methods of FSI techniques are discussed.

CHAPTER 4: METHODOLOGY

This section discusses the complete methodology of project which includes data acquisition, segmentation of brain tumor and brain tissue layers, 3D-reconstruction, FEM modelling and FSI methodology.

4.1 Data Acquisition

In this study, 14 sets of MRI scans of a tumor specific patients are used. MRI data is obtained from INMOL Cancer Hospital Lahore, Pakistan, with a 1.5 Tesla MRI machine; and has an image resolution of 512 mm x 512 mm x 288 mm with the slice thickness is 0.6 mm. BRATS 2018 MRI data [32] for tumor patients are also used in this study to make the dataset versatile and remove the homogeneity from the dataset. BRATS datasets have image resolution of 240 mm x 240 mm x 155 mm. Two different data sources are used to validate the results on different specification scales and subsequently showing the performance of our proposed model simulation. Figure 13 shows a sample MRI scan obtained from the tumor patient.

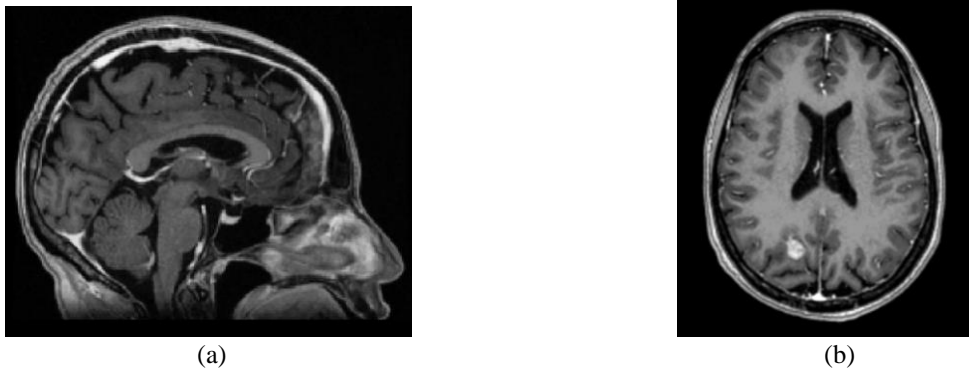


Figure 13 Raw MRI slice (a) Sagittal section of MRI scan of human brain, b) Axial section of MRI scan of human brain

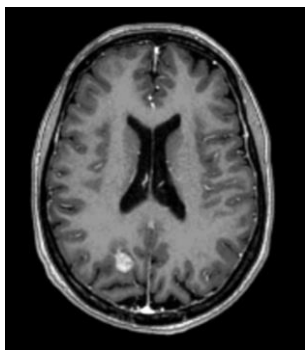
4.2 Segmentation

Brain ventricles and tumor are segmented from MRI scans, using 3D Slicer. 3D Slicer is an open-end software which provides handful of features such as thresholding, binarization, edge detection etc, for segmentation of volumetric images. To segment region of interest, thresholding operation is applied to remove pixel values which corresponds to noise and unwanted points. The thresholded

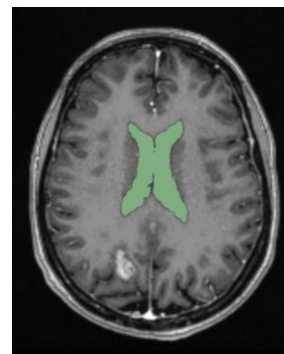
image is then smoothed using smoothing filter to remove sharp edges and spikes. Figure 14 shows the raw MRI scan and their respective segmentation. The semi-automated segmented ventricles and brain tumor masks are compared with the annotated masks (ground truth) provided by the team of expert radiologists as shown in Table I. The mean error percentage is found to be 4.75 % which shows that the proposed segmentation technique provides an acceptable level of results.

Table I Ventricular and Tumor Volume Validation Against Ground Truths

Specimen	CSF Ventricular Volume			Initial Tumor Volume		
	Segmented Volume (mm ³)	Ground truth Volume (mm ³)	Percentage error (%)	Segmented Volume (mm ³)	Ground truth Volume (mm ³)	Percentage error (%)
Datapoint 1	25320	24320	4.11%	997.29	959.51	3.93%
Datapoint 2	26940	25310	6.44%	545.36	513.41	6.22 %
Datapoint 3	26760	25080	6.69%	1300.14	1247.30	4.23 %



(a)



(b)

Figure 14 (a) T1-contrast enhanced axial scan; (b) Ventricles segmented from T1-contrast enhanced axial scan

4.3 Geometry and 3D-Reconstruction

To reconstruct data into 3D CAD models, volumetric data of brain ventricles and tumor regions are 3D-reconstructed using MIMICS innovation suite. The 3D-reconstructed geometry obtained from volumetric 2D-images usually contains unwanted noise which poses difficulty in FEM modeling and analysis. To remove the noise Laplacian smoothing filter is applied as a post-processing tool to smooth 3D CAD models as shown in Figure 15 (b) and (c). To setup the simulation, 3D-reconstructed geometry is imported in ANSYS software where, solid and fluid domains are set-up separately, CSF is modeled as fluid domain and ventricular walls as the solid domain. Fluid-solid interface boundary is created at a junction between CSF and ventricles such that the surface acts as a coupling where forces and displacements are transferred at each timestep: fluid domain transfers forces and structural domain transfers displacements to ventricular walls.

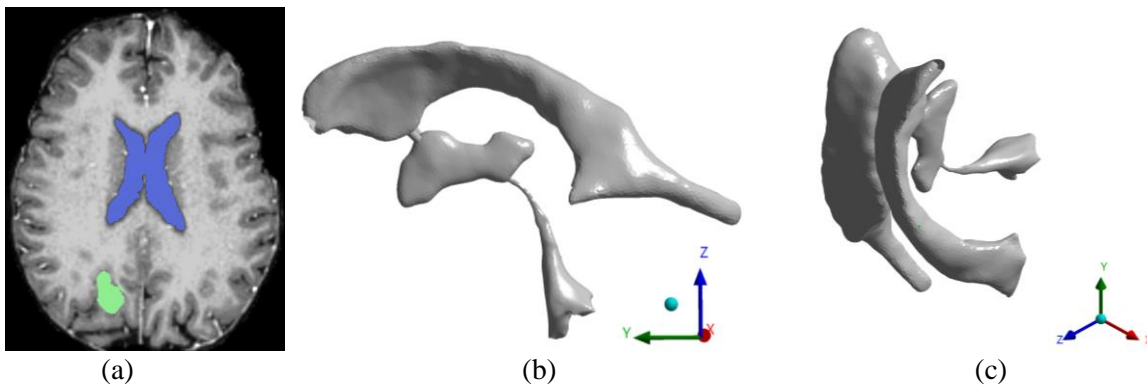


Figure 15 Representation of ventricles; (a) shows Axial section of MRI image of human brain showing ventricles and tumor; (b) shows highlighted ROI of ventricles; (b) and (c) show 3D reconstructed ventricular geometry in lateral and isometric view

4.4 Meshing

Meshing is one the most important part in FEM modeling. A good quality mesh ensures good results where as poor quality mesh brings in issues like solver divergence, singularities and poor-quality results. Structure and fluid domain are meshed separately.

4.4.1 Structural Mesh

The structural domain is meshed using shell elements (SHELL 181) are used with the thickness of 0.1 mm. Shell elements are inherently 2D elements with the thickness in user assigned direction as shown in Figure 16. These elements are computationally less expensive than solid 3D elements due to lesser number of nodes.

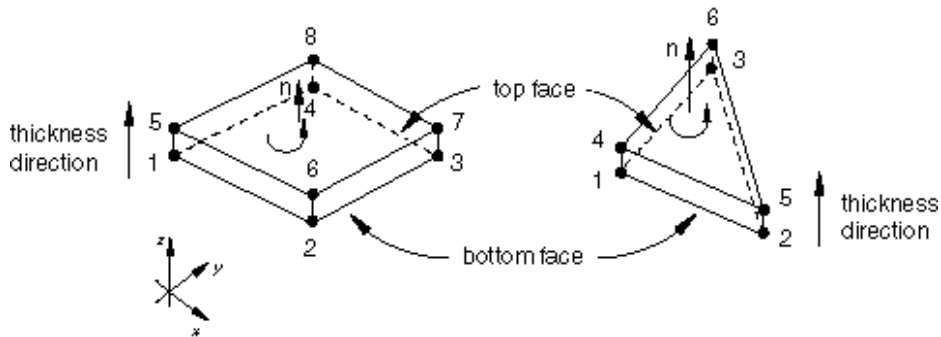


Figure 16 Shape representation of a shell element¹

Mesh independence study is performed on structure side to find the ideal mesh size. Ventricles walls are chosen as the region of interest across which average stress is noted for each mesh size and respective number of elements. Results from mesh independence study suggests that 196576 number of elements and element size of 0.1 mm are the optimal point below which grid size almost remain constant and no further variation is found in the convergence of stress. It can be seen from the Figure 17 that the grid size chosen is sufficient enough to capture all the important features such as deformation and stresses especially around the cerebral aqueduct and third ventricle.

¹ <https://abaqus-docs.mit.edu/2017/English/SIMACAEELMRefMap/simaelm-c-shelloverview.htm>

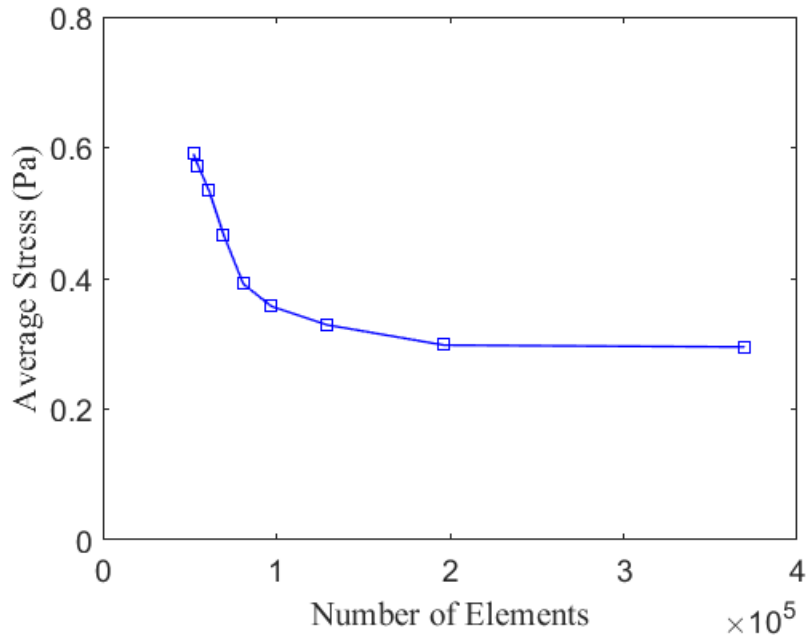


Figure 17 Mesh convergences of structural domain

4.4.2 Fluid Mesh

Meshing of fluid domain for CFD and FSI analysis plays an important role. A poor-quality mesh will lead to singularities in simulation and then ultimately solvers divergence.

Tetrahedral elements (SOLID 186) are used for meshing of fluid domain due to complex geometry and these elements can better capture complex and intricate features. Figure 18 shows the scaled-up image of a mesh around the junction point of cerebral aqueduct and third ventricle.

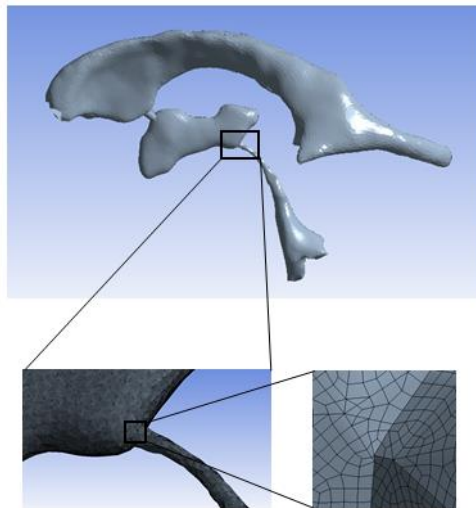


Figure 18 Finite element model mesh

Mesh independence study is performed to find out an ideal grid size where solutions converge. Peak velocity across the cerebral aqueduct and third ventricle is chosen as the parameter and region of interest as the diameter of cerebral aqueduct is small and velocity changes are prominent in this region. From mesh independence study the ideal grid size is found to be of 1144379 number of elements. From Figure 19 it is visible that the chosen grid size is fine enough to capture all the important information regarding peak velocity changes in the cerebral aqueduct and around the third ventricle.

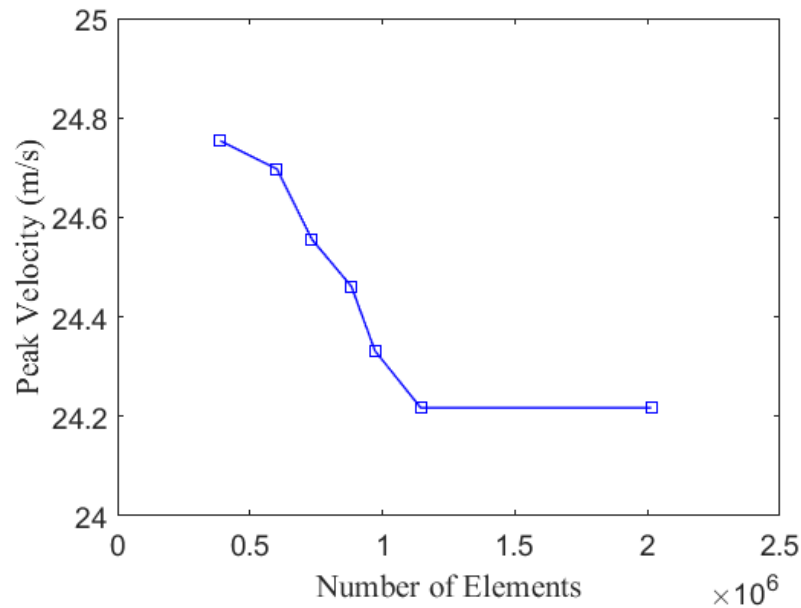


Figure 19 Mesh convergence of fluid domain

4.5 Boundary Conditions

The model consists of two inlets and one outlet, as shown in Figure 20. Mass flow inlet boundary condition with bulk production of 500 ml/day (or 6.25×10^{-6} kg/s) is used to mimic the real scenario of CSF flow.

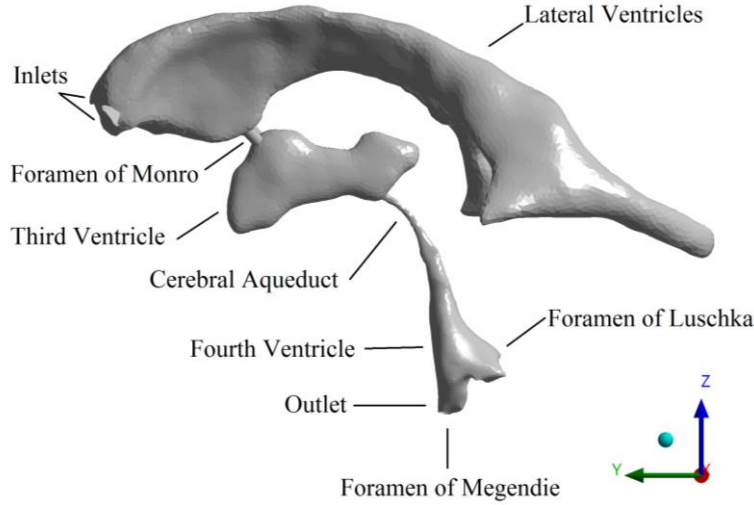


Figure 20 Boundary condition diagram

As velocity depends upon the mass-flow rate and in reality, there is a pulsatile component due to cardiac-induced systole-diastole movement, a sinusoidal function of time is also included to mimic the changing nature of the velocity within ventricles; a formulation for sinusoidal component as used by [21], is provided as follows:

$$Q_t = Q_c + Q_p \quad (6)$$

where Q_t is the total volumetric production of CSF, Q_c is the bulk or constant production rate equal to 6.25×10^{-6} Kg/s, and Q_p is the pulsatile component.

Pulsatile component in (6) takes the form as given by (7):

$$Q_p = \gamma \left(\sin\left(\omega t - \frac{\pi}{2}\right) - 0.5 \cos(2\omega t - \pi) \right) \quad (7)$$

where, γ is the amplitude of the pulsation of CSF, ω is the angular frequency.

While at the outlet, zero-gauge pressure boundary condition is used to make sure that the outlet remains at a fixed static pressure. CSF is treated as Newtonian fluid with a density of 1000 kg/m^3 and a viscosity of 0.00103 Pa.s [21]. No slip condition is used with the walls. Ventricular body is modeled as a deformable body, having modulus of elasticity of 30 KPa , Poisson's ratio of 0.49 and density of 1000 kg/m^3 . Inlets and outlets are fixed (all translations and rotations fixed) on the

structure side and the surface Ω_S is assigned as the fluid-solid interface. Table II shows the boundary conditions.

Table II Boundary Conditions

Boundary Conditions	Value	Reference
CSF Density	1000 kg/m ³	Masoumi et al [18]
CSF viscosity	0.001003 Ns/m ²	Redzic et al [19]
Bulk mass flow	6.25x10 ⁻⁶ kg/s	Wright et al [20]
Pressure outlet	Zero Pascal	L. Howden et al [10]
Modulus of Elasticity	30 KPa	Masoumi et al [18]
Ventricles Tissue Density	1000 kg/m ³	Masoumi et al [18]
Poisson's ratio	0.49	Masoumi et al [18]

4.6 Tumor Growth Model

Brain tumor is segmented from the MRI scans. To study the effect of brain tumor growth on brain ventricles over the period of time, the brain tumor growth scheme is devised. The tumor volume after certain amount of days are predicted using Gompertz [33] model which is widely used models to extrapolate tumor cells based on the initial tumor volume. The model has the solution in the exponential form in (8) as:

$$V(t) = V(0)e^{\frac{\alpha}{\beta}(1-e^{-\beta t})} \quad (8)$$

where, $V(0)$ is the initial tumor volume, α and β are the initial proliferation rate and the exponential decay constants, respectively and t is the time in days.

H. Murphy et al [34] performed a similar tumor growth model study based on the dataset of [35] and has reported constant values for different growth models. Authors have evaluated the efficiency of various Ordinary differential equations (ODE's) based models of tumor growth and

have fitted the data to find the optimum value of these constants. As the efficacy of these models on humans is still an ongoing effort and needs to be gauged objectively because of the inadequacy of in-vivo measurements of tumor size over time, various studies such as those aforementioned, however have mostly relied on animal studies such as those done on mice et cetera. to find constant values. While experimentally these growth constants may not actually depict about the exact nature of tumor growth in humans, nonetheless they do provide valuable insight and a starting point in studying tumor growth pattern. The constants are provided in Table III. Based on the extrapolated tumor volumes. Figure. 21 shows growth of tumor volume over thirty-five days; thereafter, growth remains constant.

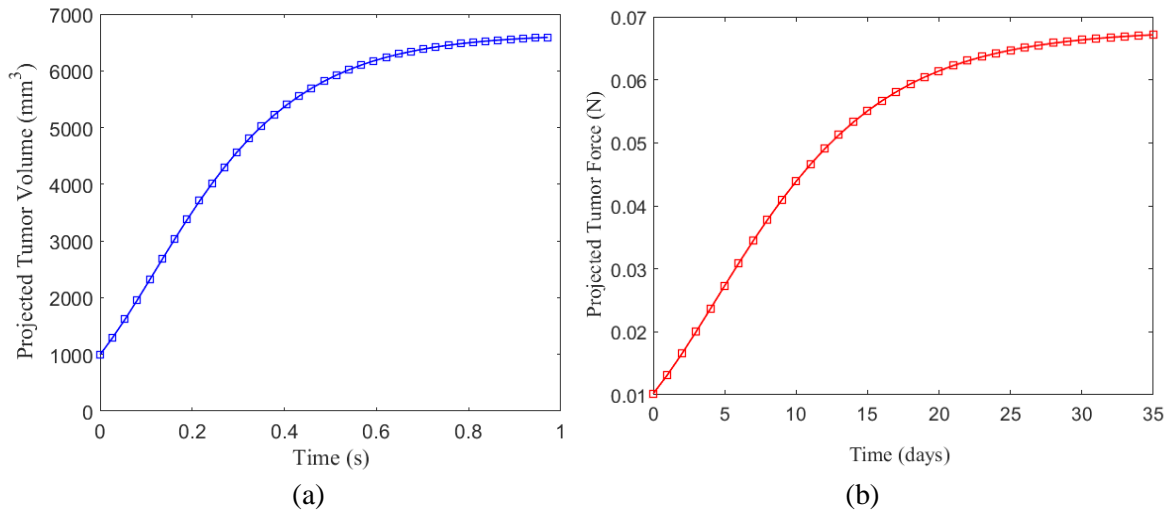


Figure 21 Predicted tumor growth (a) volume (b) force

Generally, tumor content is not fully a solid core, it also contains hydrostatic forces of fluid. However, for simplicity we have ignored the action of fluid forces and have only considered the solid core (which is also the extracellular matrix of the tumor). Body forces is one parameter which can address the concern of finding the forces of solid tumor core. Body forces can be thought of forces acting on entire volume of body such as those of electric fields or forces due to the gravity. Forces due to gravity are basically the weight of the body and can be given by equation (9) as:

$$F = \int_V \rho g dV \quad (9)$$

where F is the body force, ρ is the density of the tissue, g is acceleration due to gravity and dV is the volume differential element.

Table III gives the complete details of calculated body forces for the specified data-points. Lastly, tumor forces from all the datapoints can be either applied on the lateral ventricles or on third ventricle to record their effect on fluid flow. In this study, tumor forces are applied on the third ventricle where the effects of tumor may have greater influence on the CSF flow.

Table III Calculated Tumor Volume and Force

Specimen	Parameters	Final Calculated Tumor Volume (mm ³)	Maximum Calculated Force (N)
Datapoint 1	t = 35 days	4202	0.0467
Datapoint 2	$\alpha=0.279/\text{day}$ $\beta=0.183/\text{day}$	2498	0.0254
Datapoint 3		5956	0.0607

4.7 Numerical Simulation

Numerical simulation consists of application of various mathematical equations and predicting a response thereof. With the advent of computational modeling, solving complex models containing non-linearities have become relatively easier. In scenarios consisting of fluid-solid mechanisms such as the one at hand, the underlying case is a multi-physics problem embedding both CFD and Structural simulations. In subsequent paragraphs of the section, the simulation setup of the entire problem is described.

4.7.1 CFD Analysis Setup

To solve the flow equations Fluent is used which uses Finite Volume Method (FVM) (by assuming a control volume in which flux remains conserved—taking divergence of flux equals to zero) which, in principle, converts or reduces all the partial differential equations into a set of linear simplified algebraic equations. The underlying principles of any CFD solver primarily base on the Navier-Stokes' equation. The NS equation fundamentally rest on solving the continuity and conservation of momentum equation (11) given as below:

$$\nabla \cdot (\rho \cdot \vec{v}) = 0 \quad (10)$$

where ρ is the density of fluid, v is the velocity of the fluid, ∇ is the gradient operator

$$\rho \frac{\partial \vec{v}}{\partial t} + \rho(\vec{v} \cdot \nabla)\vec{v} = -\nabla P + \tau\rho + \mu\nabla^2\vec{v} \quad (11)$$

where $\rho \frac{\partial \vec{v}}{\partial t}$ is the local acceleration of fluid particles, $\rho(\vec{v} \cdot \nabla)\vec{v}$ is the convective acceleration, ∇P is the pressure gradient, $\tau\rho$ are body forces, $\mu\nabla^2\vec{v}$ is the viscous term which resists the motion of the fluid particles

In (11) local acceleration is the change in velocity at a given point in a flow field; whereas convective acceleration is the change in velocity due to change of position of fluid particles in a fluid flow due to any unsteadiness along the streamlines.

Solving above equations numerically requires spatial discretization and pressure-velocity coupling schemes which can be used to interpolate pressures at the faces of a control volume. In the proposed simulation, Density-Based Solver is used with all the flow regimes regardless of the flow specification; solves continuity, momentum and energy conservation equations at the same instance. Flow discretization scheme used is second order upwind; whereas for gradient discretization least-square cell-based method is used. Implicit formulation is used in discretizing equations and equations are linearized and solved iteratively using present and previous values. This results into N equations for each cell. An implicit equation solver, based on Incomplete-Lower-Upper (ILU) factorization scheme, together-with Algebraic Multigrid method (AMG), is used to speed up the convergence of the solution. F-Cycle Multigrid method is used with a termination criterion of 0.1. For transient simulations, implicit time marching scheme is used using second order backward Euler derivative formulation, in conjunction with an additional stability criterion based on Courant-Friedrichs-Lewy number (CFL). It is calculated by (12) as:

$$CFL = \vartheta \frac{\Delta t}{\Delta x} \quad (12)$$

where ϑ is the velocity, Δt is timestep size and Δx is the smallest cell size of control volume.

4.7.2 Dynamic Meshing

Due to deformable boundary the elements can get distorted and thus losing their ideal shape, therefore dynamic meshing is needed so that the moving cells can be re-meshed correctly thereby preserving shape quality. Remeshing is used to keep the mesh parameters such as skewness, aspect ratio and orthogonal quality in acceptable quality range. Diffusion-based smoothing is used to smooth deforming cells. Following equation is used for smoothing.

$$\nabla \cdot (\gamma \nabla \vec{u}) = 0 \quad (13)$$

$$\gamma = 1/d^a \quad (14)$$

where γ is given as $1/d^a$ with d being the normalized boundary distance and a is the diffusion parameter and \vec{u} is the mesh displacement velocity.

4.7.3 Structural Mechanics Setup

The structural domain is discretized into finite elements where equations are solved at nodes and interpolated at faces. The fundamental equation is given as below.

$$\{\sigma\} = [E]\{\varepsilon\} \quad (15)$$

where E is the elastic stiffness matrix, ε is the strain vector and σ is the stress vector.

Newmark Integration scheme is used to solve equations because the model generated in our scheme has non-linearities in it, therefore implicit solver is needed to reach towards a solution in an iterative manner. To judge the convergence of solution Newton-Raphson method is used which is given as below:

$$x_{n+1} = x_n - \frac{f(x_n)}{f'(x_n)} \quad (16)$$

Above equation is used to converge forces, moments and displacements at each time-step, which works by the principle that the energy added due to the external loads must eventually balance the energy induced by the reaction forces.

4.7.4 FSI Coupling Mechanism

Once the individual solvers and domains are setup, system coupling is used to exchange data at each time-step to ensure strong coupling mechanism. Two popular methods for FSI coupling mechanisms are monolithic methods and partitioned methods [36]. Monolithic schemes provide standalone FSI simulation within single solver. Partitioned methods base their physics on solving solid and fluid domain independently of each other and coupling them via interpolating scheme at fluid solid interface Ω_S . The coupling interface must satisfy two important conditions i.e., the kinematic coupling condition and the dynamic coupling conditions [37]. The kinematic coupling condition concerns with the coupling of kinematic quantities such as velocity. The dynamic coupling conditions provide necessary conditions for forces to balance at the coupling interface. In case of ventricles, the thin shell structure serves as the fluid-structure interface. In the proposed scheme, the kinematic coupling condition is no slip condition.

4.7.5 Time-Step Size and Convergence Criterion

To ensure true convergence, timestep needs to be same in both the solvers so that data exchange occurs at same instance. To this end, we have calculated timestep size based on the complexity of small-scale physics. A possible scenario for calculating a reasonable time-step size is by considering the cardiac-induced pulsations which would amount to taking smallest time-step size which is calculated as below.

$$\Delta t = 1/20f \quad (17)$$

where Δt is the time-step size, and f is the frequency of heart beats.

For a normal case, heartbeat ranges from 60-100 bpm. Equivalent frequency of 60 bpm equals 1 Hz and using (17) Δt equals to 0.05s. In this study we have taken a time-step of 0.01 seconds which is smaller than the above calculated threshold to capture small changes in the simulation.

In FSI simulations executed using partitioned methods, convergence is an important variable which merits major focus. Local convergence in both structural and fluent solvers, and global convergence in the system coupling matter since it is probable that solvers may independently be converging but may not be converging inter se. System coupling toolbox of ANSYS provides coupling iterations within each timestep so that not only both solvers get converged but also a

relative convergence tolerance is achieved, which in our case is set to 0.0005; while 5 coupling iterations are used per timestep with end time set to 4 seconds.

4.8 Summary

This chapter describes the

- Complete methodology followed in the research.
- Improved boundary conditions compared to past studies are used.
- Tumor growth model is described.
- Numerical methods setup is described in detail.

CHAPTER 5: RESULTS AND DISCUSSION

5.1 Model Validation

For anatomical data of real patient, ventricles are segmented from 3D T1-contrast enhanced MRI images; similarly, tumor regions are segmented manually. Segmented ventricular volumes are validated against the ground truths provided by the radiologist. For Datapoint B and C ground truths for ventricular volumes are labelled by the radiologist, whereas the ground truth for tumors are already provided by the training dataset of BRATS 2018 [32]. Table I summarizes the findings in this regard.

5.2 CSF Flow Properties

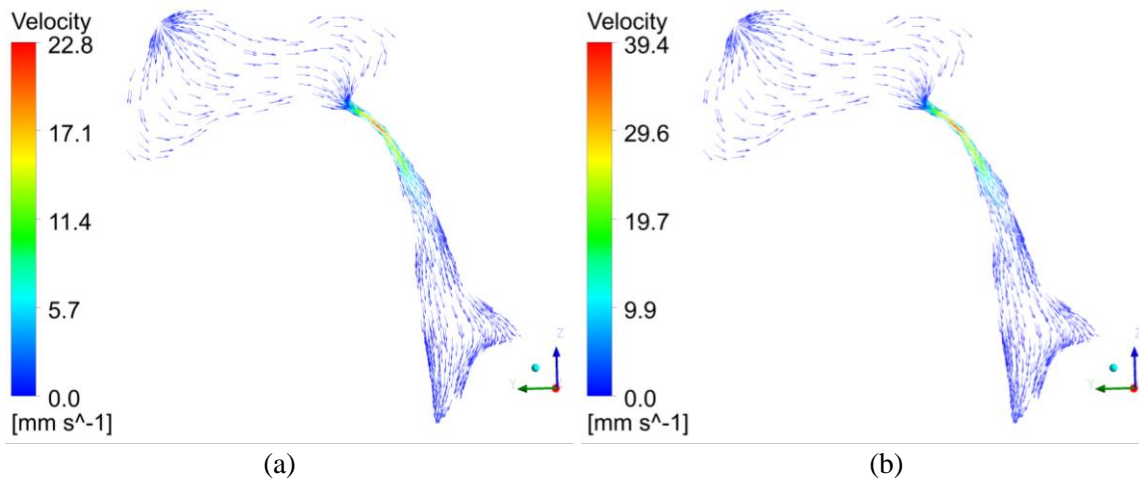


Figure 22 Velocity vector plots in third and fourth Ventricle; (a) represents the case of no tumor, and (b) represents the case with tumor

The results obtained from CFD analysis are presented in Figure 22. Peak CSF velocity occurs in the aqueduct of Sylvius due to narrowing of pathway. Findings of present study show that CSF velocity values in the aqueduct rise to a greater value and remain almost same in the foramen of Monro and lateral ventricles. As clear from figure 22 (a), maximum velocity of 22.84 mm/s occurs in aqueduct when no external forces are applied; while for the case of tumor it rises to 39.40 mm/s as shown in Figure 22 (b) indicating a rise of 72.50 %. This change in velocity is one of the significant parameters which qualitatively defines the CSF flow field, especially in the cerebral

Table IV Calculated Tumor Volume and Force

Specimen	CSF velocity in cerebral aqueduct			Reynold's number		Womersley number
	Without tumor (mm/s)	With tumor (mm/s)	Percentage change	Without tumor	With Tumor	
Datapoint 1	22.84	39.40	72.50	41.0	70.7	5
Datapoint 2	24.31	41.75	71.74	52.1	89.5	5.38
Datapoint 3	28.97	51.70	78.46	60.47	107.91	5.75

aqueduct where most changes take place. Table IV shows the results obtained from Datapoint 1,2 and 3. Mean rise in velocity for cases of tumor is found out to be 74.23%.

Reynold's number is an important parameter which signifies the transition of flow from laminar to turbulent. It is defined as the ratio of fluid inertial forces to the viscous forces, and is a metric used to differentiate whether CSF, in localized region such as aqueduct, remains laminar or turbulent. It is given as:

$$Re = \frac{\rho \vartheta L}{\mu} \quad (18)$$

where L is the characteristic length which is taken to be the diameter of the aqueduct, μ is the dynamic viscosity of fluid, ρ is the fluid density and ϑ is the velocity of the CSF in aqueduct.

Based on the above findings (see Table IV), maximum Reynold's number across normal cases is 60.47; and for tumor case it rises to 107.91. Overall flow remains in the laminar regime, but in localized sections, velocity gradients are abrupt. Transition of CSF from creeping flow towards a relatively high local Reynold number flow is evident for both cases. First, CSF flows from the lateral ventricles and passes into the foramen of Monro. Here the velocity changes are insignificant and almost remain a creeping flow. It also remains the same for the tumor case as well in lateral ventricles. Vortices of small magnitude also appear in the third ventricle. When CSF enters into the cerebral aqueduct region, velocity starts to rise and reaches up to 22.84 mm/s for normal case, and for tumor case it reaches up to 39.4 mm/s clearly showing that the flow no longer,

at least in the localized region of the cerebral aqueduct, remain strictly under the characterization of a creeping flow. Post aqueduct, velocity in the fourth ventricle drops and flow goes back towards a relatively creeping flow regime. Reynold's number throughout the ventricular domain remains under 0.015 showing that the flow by and large remains a creeping flow. Major oscillations in flow field are observed in the cerebral aqueduct. The rise in velocity of around 16.56 mm/s indicates that once the brain parenchyma interaction is considered the velocity may sharply rise, and possibly may also cause stenosis of aqueduct thereby resulting obstructive hydrocephalus.

5.3 CSF Flow Field Pulsatility

To calculate pulsatile nature of flow field, Womersley number denoted by α is used. Womersley number is a dimensionless number and a metric used to signify the pulsatile nature of the biofluid in relation to the flow viscous effects [38]. It is given by (19) as:

$$\alpha = L \sqrt{\frac{2\pi\rho}{T\mu}} \quad (19)$$

where L is the characteristic length, T is the time period of the heartbeat oscillations, ρ is the fluid density and μ is the dynamic viscosity of the fluid. In case of ventricular system, characteristic length L is taken to be the diameter of aqueduct which affects the flow field significantly, α is calculated for all the datapoints as shown in the Table IV. For values of $\alpha \geq 1$ the flow field is sinusoidal in nature. Across all the datapoints, calculated Womersley number is greater than one, suggesting that the flow is pulsatile in nature.

5.4 Flow Parameterization under Cardiac cycle

As stated earlier, pulsatile mass flow inlet boundary condition is used using (6) and (7). To visualize the effects of cardiac cycle and systole-diastole effects, the entire simulation is executed for 4 seconds. Figure 23 shows the output of pulsatile component of mass flow rate, peak pressures in the lateral ventricles, and CSF velocity in the cerebral aqueduct. Human heart acts as a pumping machine and through entire cardiovascular system it supplies blood to all parts of body. Carotid arteries are the supply lines for blood towards brain. Since heartbeat is continuous and is usually rhythmic and periodic, pulsations in blood are formed which also affect the CSF movement in the ventricles and subarachnoid space. Every beat induces a to and fro motion of CSF in the ventricles.

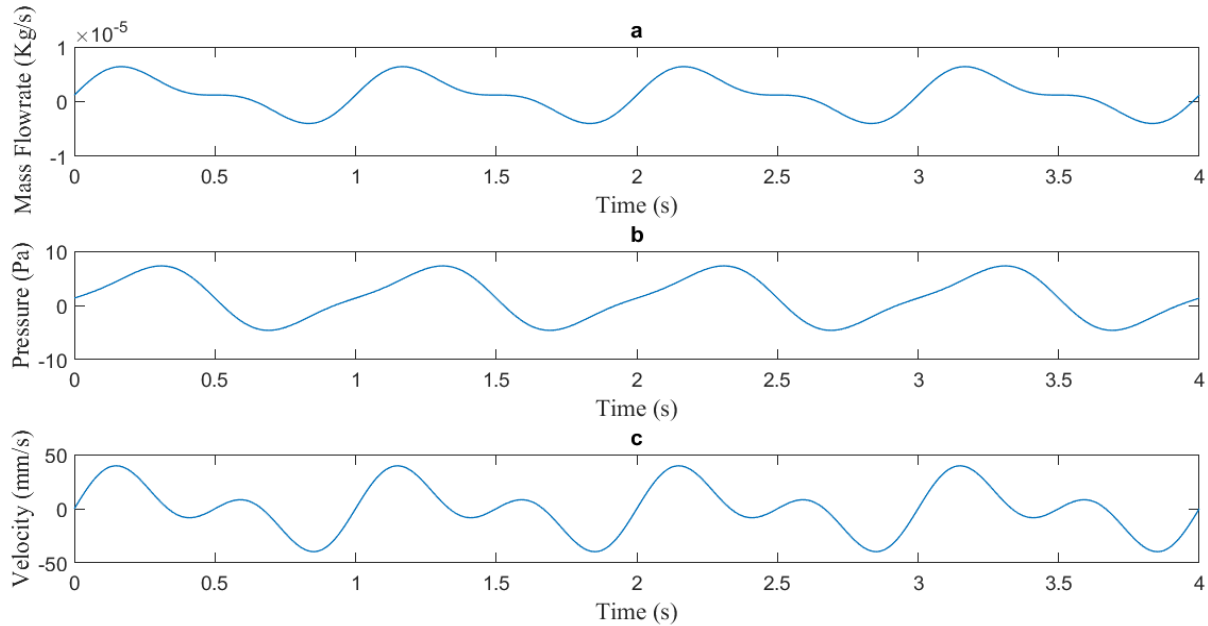


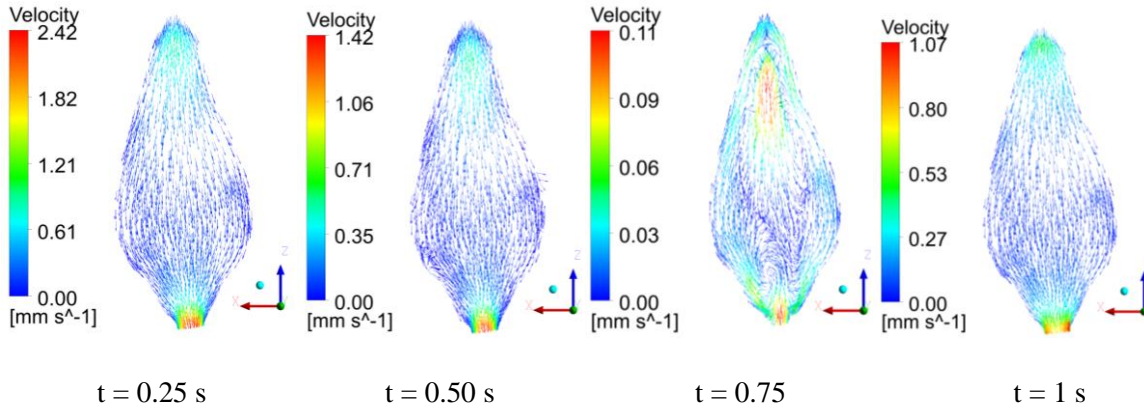
Figure 23 Pulsatile mass flowrate at inlets; Peak pressures in the lateral ventricles, and CSF velocity in cerebral aqueduct.

This motion is usually modeled by taking it as combination of sinusoidal waves whose frequency is equal to the frequency of heartbeat. Peak systole represents the maximum pressures the heart applies to supply blood to various parts of the body, and peak diastole is point where heart relaxes and refills the blood in its chambers. As visible from the Figure 23, the maximum velocity occurs at approximately 17% (where frequency of beat is taken 1 Hz therefore, in window of 0-1 seconds, 17% corresponds to time of 0.17 seconds) of systole and the minimum velocity occurs at about 84% of the diastole.

5.5 Reverse Flow in Fourth Ventricle during Cardiac Systole-Diastole

CSF flows back and forth in the ventricles in a cardiac cycle. During systolic pressure, the brain parenchyma is squeezed and therefore lateral and third ventricles are compressed thereby forcing the CSF movement craniocaudal [40] towards the spinal canal and in subarachnoid space; at this instance velocity is on the higher side even in the cerebral aqueduct and in the fourth ventricle. Figure 24 shows velocity two cases: case A refers to normal case and case B refers to a tumor case. At time steps 0.25 and 0.5 for case A, one can see that the velocity peaks at 0.25s, and post 0.5s, the diastolic phase starts, and velocity starts to reverse; timesteps of 0.75s and 1s show that velocity starts to dip and then peaks again respectively. The same is repeated for case B, albeit with a significant rise in the velocity.

CASE A: Without Tumor



CASE B: With Tumor

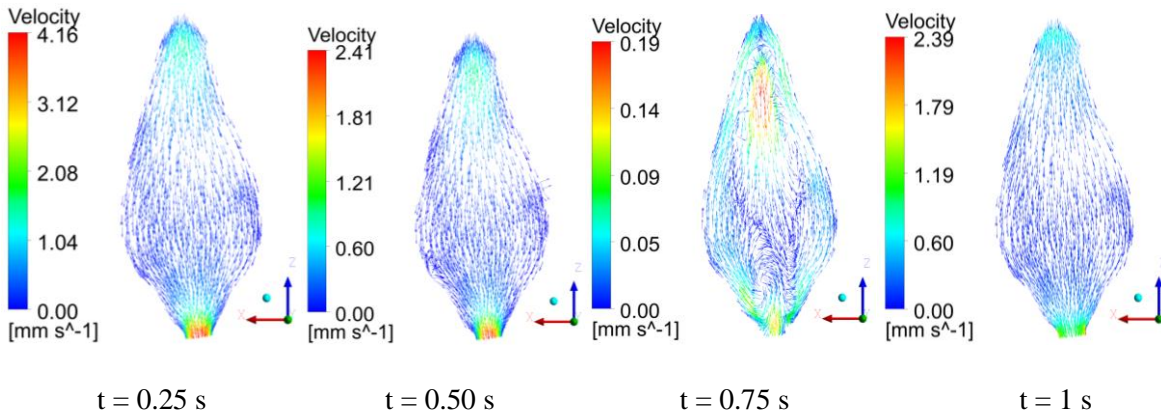


Figure 24 Visualization of velocity vectors in fourth ventricle at various timesteps. Case A represents velocity vectors in fourth ventricles for without tumor; and Case B represents velocity vectors in fourth ventricles for tumor.

5.6 Pressure Field

Pressure changes in the ventricular wall when considered completely with the brain parenchyma represent intracranial pressures. Pressure variations in large cavities such as lateral ventricles are negligible and found to be spatially uniform. Figure 25 (a) and (c) shows the pressure field for normal and tumor cases. Maximum pressures under the normal case are 4.35 Pa in the lateral ventricles. Pressure drop of 0.1 Pa is found in the third ventricle, while across the cerebral aqueduct it is found out to be 2.88 Pa. While for the tumor case, maximum pressure of 7.1 Pa is

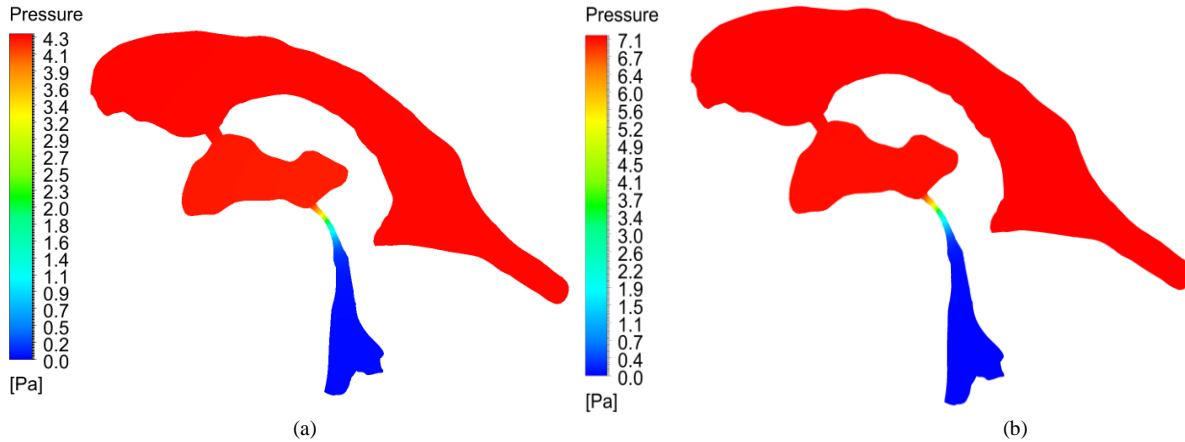


Figure 25 Pressure on ventricle wall. (a) shows pressures without tumor; and (b) shows pressure under tumor forces

found in the lateral ventricles, with a pressure drop of 0.25 Pa in the third ventricle. Pressure drop in the cerebral aqueduct is found out to be equal to 4.74 Pa. A large pressure drop in the cerebral aqueduct shows a higher velocity rise.

5.7 Total Deformation of Ventricles

The deformation due to the interaction of fluid forces and tumor across the walls of ventricles are recorded as shown in Figure 26 (b) and (d). For normal case the peak deformation in our study is found to be 2 μm , whereas for tumor case the peak deformation is found across third ventricle which came out as 11 μm . This deformation is passed on to the CSF domain, where relative displacement of walls inwardly causes a rise in CSF flow velocity in third ventricle and in cerebral aqueduct. Table V summarizes results in this regard.

Table V Deformation comparison with and without the influence of tumor

Specimen	Peak Deformation		
	Without tumor (mm)	With tumor (mm)	Increase in Deformation (mm)
Datapoint 1	0.0021	0.011	.0089
Datapoint 2	0.0032	0.016	.0128
Datapoint 3	0.0055	0.029	.0235

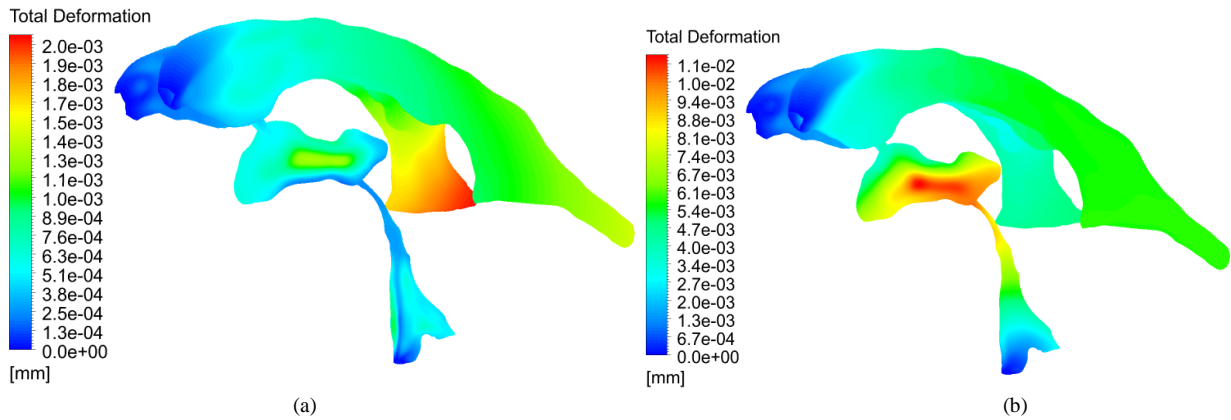


Figure 26 Deformation of ventricle wall. (a) shows deformation without tumor; and (b) shows deformation under tumor forces

5.8 Comparison of Results

The results obtained from the proposed methodology are compared against the literature as shown in Table VI. Hereinbelow, the results are compared against two group of studies. First group corresponds to the numerical FSI studies done in past on the same connected matter and results herein are validated against these and second group corresponds PC-MRI studies which have also produced results regarding flow velocity of CSF et cetera.

In all cases, peak CSF velocity is under the range reported by the proposed technique. For tumor, there are no established studies, hence we can resort this problem intuitively. Likewise, as evident from Table VI, our proposed model is not only compared against all the reported data in literature but also goes one step ahead. In studying CSF flow and biomechanical behavior, most researches in literature do not cater the deformable character of ventricles (excluding Masoumi et al [21]) and mostly rely on mere simple CFD-based flow modeling. However, our findings suggest that this assumption is not founded on firm roots and our proposed fully coupled FSI based model provides complete description of how ventricle and CSF interact dynamically. Second, based on this, we can easily infer that the proposed model can now (since it is fully two-way FSI) be used for various cases such as stenosis of cerebral aqueduct, effect of cerebral edema or hematoma on CSF flow et cetera.

Table VI Comparison of results obtained from the proposed method against previous studies

Study	Velocity in CA (mm/s)	Pressure Drop (Pa)	Deformation (mm)
Jacobson et al. (1996) [14]	28	<1.1 for CA	Walls modeled as rigid
Fin and Grebe (2003) [15]	64.65	2.91 for elastic wall model for CA	Implemented flexible cylindrical wall model of CA and obtained 0.61 mm deformation
Linninger et al. (2005) [16]	25.8/-21.7	2 in CA	No deformation reported. However, net increase of ventricular volume of 4.5% is reported.
Kurtcuoglu et al. (2007) [17]	120	20	No deformation reported
Howden et al. (2008) [19]	11.38	1.14	Walls modeled as rigid
Masoumi et al. (2010) [20]	18/-15	<5	No deformation reported. However, net increase of ventricular volume of 6% is reported.
Masoumi et al. (2013) [21]	8/-6	< 2	Normal CSF-Ventricular interaction under normal case: 0.006 mm
PC-CINE: Abbey et al (2009) [41]	32.4±1.08	-	-
PC-CINE: Algin et al (2010) [42]	47.8±2.48	-	-
PC-CINE: Lee et al (2004) [43]	33.9±1.61	-	-
Proposed Method	Normal case: 22.8 Tumor case: 39.4	Normal case: 2.88 Pa across CA Tumor Case: 4.74 Pa across CA	Normal case deformation= 0.002 mm Early tumor interaction deformation= 0.011 mm

5.9 Statistical Analysis

To establish the correlation between cerebrospinal fluid and tumor, a statistical study with 14 participants is carried out as shown in Table VII. The effect of brain tumor on the deformation of brain ventricles and the cerebrospinal fluid velocity is studied using ANOVA analysis.

Table VII Patient data for statistical study

Patient	Initial Tumor Volume (mm³)	Predicted Tumor Volume (mm³)	Predicted Tumor Force (N)	Normal Deformation (um)	Tumor Deformation (um)	Normal Velocity (mm/s)	Tumor Velocity (mm/s)
1	997.29	6590	0.0672	2.1	11	22.8	39.4
2	545.36	7704	0.0768	3.2	16	24.3	41.7
3	1300.14	8592	0.0877	5.5	23.5	28.9	51.7
4	5668.38	36745	0.3749	14.4	838	27.5	77
5	6364.87	42000	0.4285	26.2	2035	30.1	150
6	4201.93	27728	0.2829	25.6	1728	28.5	123
7	5591.24	36896	0.3764	17.8	900	35.5	85
8	2782.10	18359	0.1873	13.1	175	11.4	77
9	3637.76	24005	0.2499	7.4	184	16.2	95
10	6260.88	41315	0.4215	34.3	1115	24.0	110
11	8289.63	54702	0.5581	40.7	3000	36.6	278
12	5041.27	33267	0.3394	33.8	1300	21.7	134
13	7539.05	49749	0.5076	22.5	2100	29.3	164
14	7609.03	50211	0.5122	27.8	2600	33.4	210

5.9.1 CSF Velocity Correlation with Tumor

From Figure 27 we can see that without the presence of tumor forces the velocity in subjects remains in the range of 20-30 mm/s whereas for tumor specific subjects the velocity in ventricles due to the tumor force significantly rises. This draws the conclusion that tumor inside the brain significantly disturbs the hemostasis by increasing the velocity of cerebrospinal fluid.

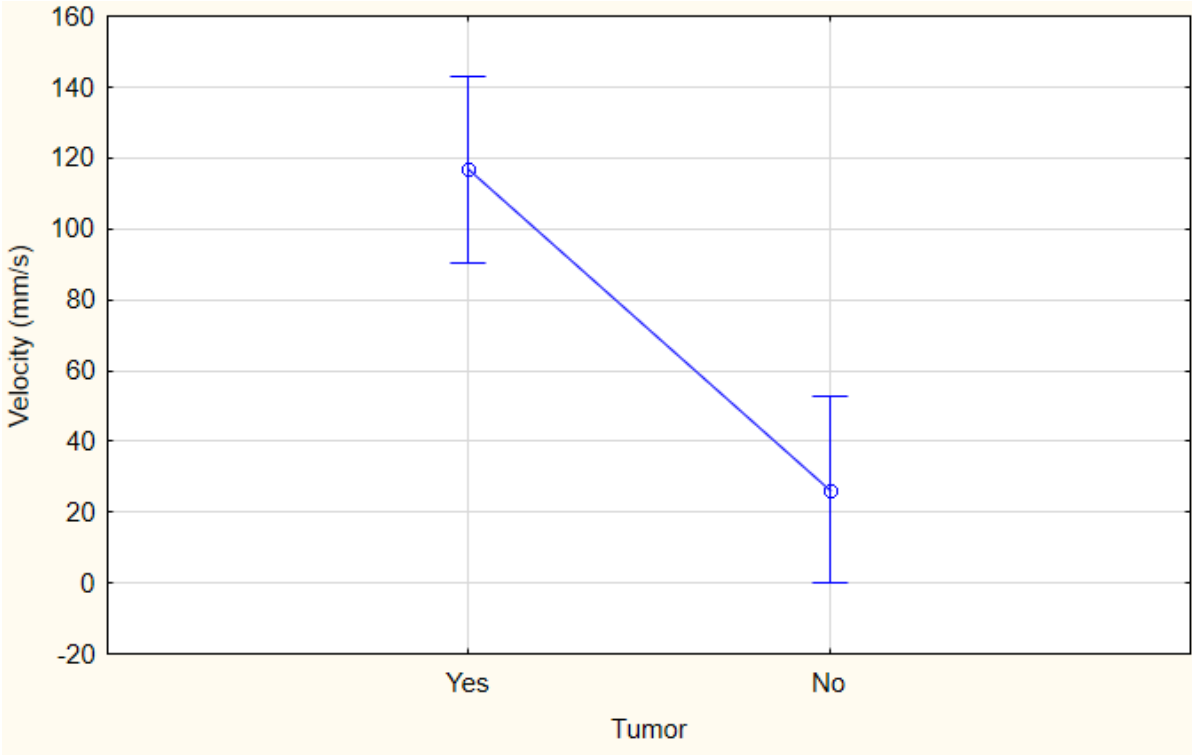


Figure 27 ANOVA analysis, CSF Velocity vs Tumor

5.9.2 Deformation Correlation with Tumor

From Figure 28 we can see that without the presence of tumor forces the deformation in subjects remains in the range of 2-5 μm , whereas for tumor specific subjects the deformation of ventricular walls due to the tumor force significantly increases to 1000-1500 μm . This study shows that the tumor in the close vicinity of ventricle exert compressive forces which significantly deforms the ventricles.

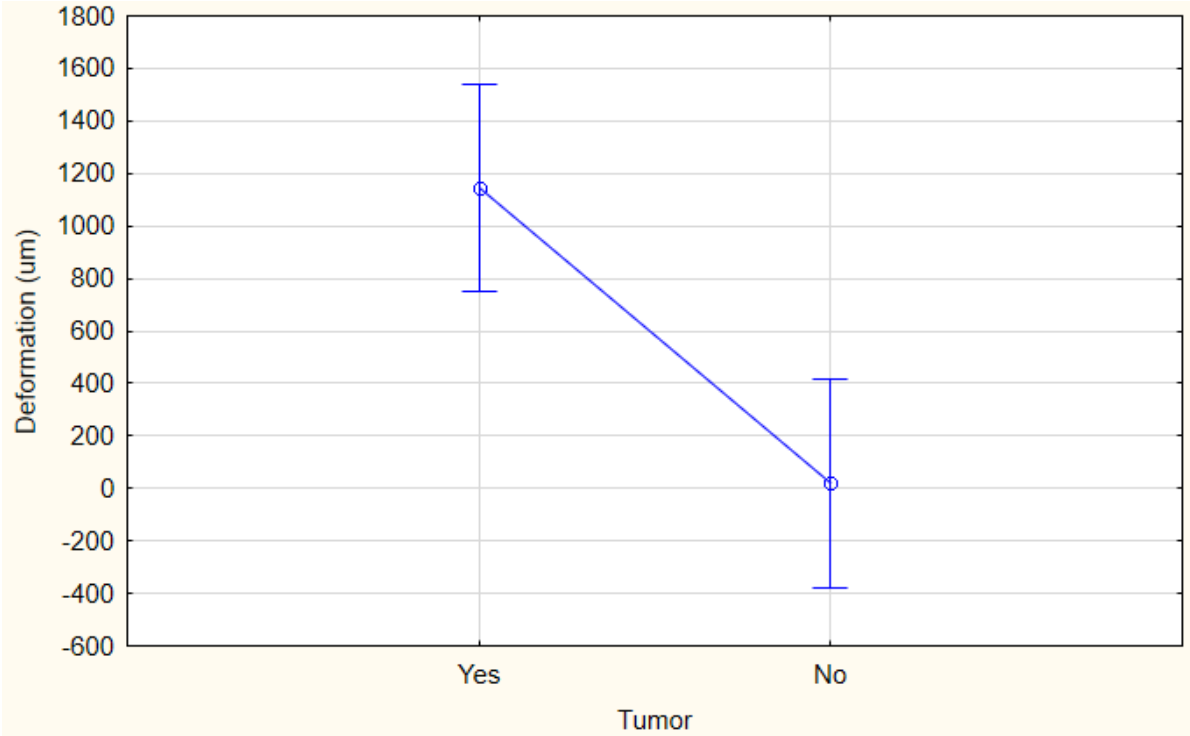


Figure 28 ANOVA analysis, Deformation vs Tumor

CHAPTER 6: CONCLUSION AND CONTRIBUTIONS

6.1 Conclusion

This thesis is one of the first attempts at modeling the CSF flow through the brain ventricles under the influence of brain tumor. By choosing to model the structure and fluid regimes using two-way Fluid-structure interaction, a complete understanding of the underlying dynamics of CSF flow in ventricles is presented. The proposed methodology considers all the relevant and major physiological factors which may markedly influence the CSF flow in the ventricles. These inter-alia include cardiac cycle induced pulsations, dynamic interactions between the deformable wall of ventricles and flow profiles, backflow of CSF in diastole; and most importantly, the influence of brain tumor on physiological flow parameters of CSF. Among all the datapoints used in this research, one clearly observes that under the case of brain tumor mean CSF velocity increases about 74.2%, which clearly shows the influence of brain tumor on CSF flow parametrization. Maximum local Reynold's number in the cerebral aqueduct reaches up to 107.91 which shows that the flow transition in the cerebral aqueduct is rather abrupt due to the narrow pathway. Furthermore, the proposition that the flow of CSF throughout the domain by and large remains a creeping flow is validated through this study as well. CSF flow velocity in lateral ventricles is of the orders of 10⁻³ mm/s. It is only through the aqueduct that the flow changes are maximum. Secondly, cardiac induced pulsations have an effect on the CSF flow profile mainly in the cerebral aqueduct and the fourth ventricle where backflow of cerebrospinal fluid occurs. Fourth ventricle usually experiences maximum backflow and hence during diastole velocity in craniocaudal direction reduces. This pattern repeats itself in all cardiac cycles for both tumor and non-tumor case; however, the only difference is the magnitude of velocity which is higher in case of tumor. Transmante pressures on the walls of ventricle remain under 4.3 Pascals (0.032 mmHg) for non-tumor case, whereas for tumor case, pressures increase up to 7.1 Pascals (0.053 mmHg) clearly highlighting that pressures rise during tumor case. The mean deformation of 0.0036 mm is recorded for the non-tumor cases, where no tumor forces are taken into consideration and only the fluid forces produce the aforementioned deformation. However, for the cases of tumor, mean deformation rise up to 0.0186 mm, signifying the fact that forces due to tumor constrict the ventricular wall and produce resultant increase in the CSF flow velocity. Needless to say, deformation depends upon the tumor volumes which are different in all cases, and so are the forces.

But this nonetheless provides an insight of how much effect is produced by tumor on the deformation of ventricular walls. Lastly, the instant research has dealt successfully in biomechanical modelling of CSF in human ventricular system under the influence of brain tumor. It first gives the foundational basis for modelling such scenarios using two-way FSI and then utilizing the modelling strategy it goes on to implement it for case of tumor and benchmarks it against both normal case and already reported established studies in literature. This biomechanical model of CSF in times of need for non-invasive techniques may be used by the doctors for the purpose of making informed decisions before undertaking any surgical intervention.

6.2 Research Contributions

The proposed research is the first attempt to study the human ventricular system under the influence of brain tumor. In the current research, a realistic and anatomically accurate model of human ventricle system is used. The dynamics of cerebrospinal fluid and HVS under the influence of brain tumor are modeled using a novel fluid-structure interaction approach. The proposed research has addressed all the shortcomings present in the literature. This study has introduced a new dimension of studying brain dynamics and pathologies.

Following are the main research gaps which existed in the past studies

1. In the past studies ventricles are modeled as rigid, which poses serious questions regarding their behavior in real anatomy.
2. Most studies performed does not cater the interaction of ventricular structure on the flow of CSF and vice-versa.
3. No interaction of surrounding brain tissue is reported.
4. Very few studies have worked on the pulsatility of CSF flow.

Proposed research has successfully addressed all the shortcoming of past studies as follows:

1. Ventricular walls are modelled as linearly elastic which better captures the effect of brain tumor and CSF under histological conditions.
2. The deformable nature of ventricles is studied for a normal case and tumor specific case which help clinicians to distinguish the effect of brain tumor on HVS.
3. With the help of proposed model, the interaction of HVS with surrounding brain tissue can be studied.

4. Pulsatile nature of CSF is modeled i-e the movement of CSF under cardiac systole and diastole which mimics the accurate representation of CSF physiology in real life.
5. A quantitative relation between the velocity of CSF and deformation of HVS under the influence of tumor is established.

Following are the key finding of the proposed research:

1. CSF velocity in a normal case is found to be 22.8 mm/s whereas in case of a tumor patient the velocity increases to 39.4 mm/s
2. CSF velocity increases about 74.2%, which clearly shows the influence of brain tumor on CSF flow
3. Pressures on the walls of ventricle remain under 4.3 Pa (0.032 mmHg) for a normal case, whereas for tumor case, pressures increase up to 7.1 Pa (0.053 mmHg)
4. The mean deformation of 0.0036 mm is recorded for a normal case. However, In the case of tumor, mean deformation rise up to 0.0186 mm, signifying the fact that forces due to tumor constrict the ventricular wall and produce resultant increase in the CSF flow velocity.
5. Pulsatile modeling of CSF plays an important role in the flow of CSF and as it takes into account the cardiac pulsation.
6. Deformable character of ventricular walls provides a better insight into CSF mechanics.

CHAPTER 7: LIMITATIONS AND FUTURE WORK

There is a need to highlight in the end some factors which the instant study does not take into consideration. First is the gravity factor. Gravity affects everything including flow of fluids. However, if the flow is single-phase and fluid is incompressible (which CSF is), and density changes are negligible then gravity induces little effect on the parametrization of the flow field because when there is no net change in density, the fluid forces will be exactly the same and counter-acting against the gravity forces, thus ensuring that fluid remains in equilibrium. However, since CSF movement is influenced by positioning of the person, gravity may induce an effect on the flow profile of CSF.

Second, is the little pulsations caused by respiration (similar to cardiac induced pulsations). In normal cases where breathing is normal, CSF movement is little influenced by normal thoracic breathing [39], however if deep excursions and abdominal breathing is considered then one may presume that it may induce some effect on the CSF flow [44]. Be that as it may, the dominant effect would still be coming from the cardiac induced pulsation notwithstanding if one considers the respiratory induced pulsations.

Third factor which has been ignored in the instant is that we have mainly focused on the tumor forces due to the solid core and have neglected the interstitial fluid component. Tumor's solid core is essentially made up of extracellular matrix and collagen fibers; it by far has the largest contribution towards tumor forces and can be assumed to approximate around this force. This simplification provides us a valuable insight about the interaction of tumor force on ventricles. Interstitial fluid forces can only contribute when the growing extracellular matrix has either ruptured or it has created a cerebral edema in its vicinity. Other than aforementioned, the contribution of forces coming from interstitial fluids can safely be neglected.

Fourth, for an accurate modeling, one can also consider the bulk flow production as whole by choroid plexus and may assume entire inner walls of ventricles as inlets. This assumption is not wrong (and does in fact resemble with the physiological condition). However, in modeling it numerically, it may not produce much observable difference because, as stated above, CSF flow is largely a creeping flow, hence whether one chooses entire walls as inlet or some specific points as inlets, as proposed herein (and also done by Howden et al [19], Masoumi et al [21], Linninger et al [16], Fin and Grebe [15]), would not be different than the previous case. However, for

completeness, one can take this as an additional factor in modeling FSI modeling of CSF. Fifth, since tumor produces dynamic forces all around the brain parenchyma which may well transmit till ventricles, one may assume that it may also induce effect in the bulk production of CSF in ventricles, by affecting and possible deforming choroid plexus. This may be true and relevant from a physiological aspect because if bulk flow from inlets is decreased, pressure gradients can change drastically, and a decreased CSF flow is expected.

Lastly, as stated earlier, we have modelled CSF biomechanical by segmenting anatomically realistic brain ventricles. We have not considered the effect of Subarachnoid space where 75% of CSF volume is found. The purpose of not considering in this study is the fact that the biomechanical properties, flow parametrization and Transmantle pressure distributions are largely driven or influenced by changes in biomechanical behavior of CSF in brain ventricular regions, among others, cerebral aqueduct. For instance, obstructive hydrocephalus is predominantly caused due to choking of cerebral aqueduct thereby increasing ICP; changes of CSF velocity in subarachnoid space are negligible because it is a large cavity, and thus creeping flow dominates [45]. Therefore, while analyzing CSF biomechanical character one needs to model the behavior of CSF in ventricular regions. Notwithstanding that even though in intracranial hemorrhages or in cerebral venous sinus thrombosis blockage may occur in venous discharge within brain causing increase in ICP, but that would not be due to the changing character of CSF but rather due to another cause i.e., hematoma.

REFERENCES

- [1] Russo, and C. V. Putte, Seeley's essentials of anatomy & physiology: McGraw-Hill, 2015.
- [2] W. E Arnould-Taylor, "A textbook of Anatomy and Physiology", 3rd edition, Stanley Thomas Publishers Ltd ,1977.
- [3] Cinnamon VanPutte, Jennifer Regan and Andrew Russo, "Seeley's Essentials of Anatomy & Physiology", 9th edition, McGraw Hill Education, 2016.
- [4] James Weyhenmeyer and Eve Gallman, "Rapid Review Neuroscience", Mosby Publishers, November 29, 2006.
- [5] Ben L. C. Wright, James T. F. Lai and Alexandra J. Sinclair, "Cerebrospinal fluid and lumbar puncture: a practical review", Journal of Neurology, Volume 259, Issue 8, pp. 1530-1545, August 2012.
- [6] Purves D, Augustine GJ, Fitzpatrick D, et al., editors, "The Neuroscience", second edition, Sunderland (MA): Sinauer Associates, 2001.
- [7] L. A. Steiner and P.J.D. Andrews, "Monitoring the injured Brain: ICP and CBF", British Journal of Anaesthesia, Volume 97, Issue 1, pp. 26-38, July 2006.
- [8] John M. Turner, "Intracranial Pressure", Book chapter in, "Textbook of Neuroanaesthesia and intensive care".
- [9] 2020. [Online]. Available: [www.braintumor.org/brain-tumor information/brain-tumor-facts/](http://www.braintumor.org/brain-tumor-information/brain-tumor-facts/)
- [10] 2020. [Online]. www.cancer.net/cancer-types/brain-tumor/statistics
- [11] J. Pickard, and M. Czosnyka, "Management of raised intracranial pressure," Journal of Neurology, Neurosurgery & Psychiatry, vol. 56, no. 8, pp. 845-858, 1993.
- [12] P.H. Raboel, J. Bartek Jr., M. Andresen, B.M. Bellander and B. Romner, "Intracranial Pressure monitoring: Invasive versus Non-invasive Methods—A Review", Review article published in, "Critical Care Research and Practice", Vol 2012, Hindawi Publication Cooperation, March 2012.
- [13] N. J. Alperin, S. H. Lee, F. Loth, P. B. Raksin and T. Lichtor, "MR-intracranial pressure (ICP): a method to measure intracranial elastance and pressure non-invasively by of MR imaging: baboon and human study", Radiology, Vol. 217, no. 3, pp. 877-885, 2000.
- [14] E. E. Jacobson, D. F. Fletcher, M. K. Morgan, and I. H. Johnston, "Fluid dynamics of the cerebral aqueduct," Pediatric neurosurgery, vol. 24, no. 5, pp. 229-236, 1996

- [15] L. Fin, and R. Grebe, "Three-dimensional modeling of the cerebrospinal fluid dynamics and brain interactions in the aqueduct of sylvius," *Computer methods in biomechanics and biomedical engineering*, vol. 6, no. 3, pp. 163-170, 2003.
- [16] A. A. Linninger, C. Tsakiris, D. C. Zhu, M. Xenos, P. Roycewicz, Z. Danziger, and R. Penn, "Pulsatile cerebrospinal fluid dynamics in the human brain," *IEEE Transactions on Biomedical Engineering*, vol. 52, no. 4, pp. 557-565, 2005.
- [17] V. Kurtcuoglu, D. Poulidakos, and Y. Ventikos, "Computational modeling of the mechanical behavior of the cerebrospinal fluid system," *Journal of biomechanical engineering*, vol. 127, no. 2, pp. 264-269, 2005.
- [18] E. E. Jacobson, D. F. Fletcher, M. K. Morgan, and I. H. Johnston, "Computer modelling of the cerebrospinal fluid flow dynamics of aqueduct stenosis," *Medical & biological engineering & computing*, vol. 37, no. 1, pp. 59-63, 1999.
- [19] L. Howden, D. Giddings, H. Power, A. Aroussi, M. Vloeberghs, M. Garnett, and D. Walker, "Three-dimensional cerebrospinal fluid flow within the human ventricular system," *Computer methods in biomechanics and biomedical engineering*, vol. 11, no. 2, pp. 123-133, 2008.
- [20] N. Masoumi., Bastani, D., Najarian, S., Ganji, F., Farmanzad, F., & Seddighi, A. S. (2010). Mathematical modeling of CSF pulsatile hydrodynamics based on fluid–solid interaction. *IEEE transactions on biomedical engineering*, 57(6), 1255-1263.
- [21] N. Masoumi, F. Framanzad, B. Zamanian, A. Seddighi, M. Moosavi, S. Najarian, and D. Bastani, "2D computational fluid dynamic modeling of human ventricle system based on fluid-solid interaction and pulsatile flow," *Basic and clinical neuroscience*, vol. 4, no. 1, pp. 64, 2013.
- [22] J. Tu, G. H. Yeoh, and C. Liu, *Computational fluid dynamics: a practical approach: Butterworth-Heinemann*, 2018.
- [23] F. Loth, M. A. Yardimci, and N. Alperin, "Hydrodynamic modeling of cerebrospinal fluid motion within the spinal cavity," *J. Biomech. Eng.*, vol. 123, no. 1, pp. 71-79, 2001.
- [24] H. D. Portnoy, and M. Chopp, "Cerebrospinal fluid pulse wave form analysis during hypercapnia and hypoxia," *Neurosurgery*, vol. 9, no. 1, pp. 14-27, 1981.

- [25] Hart, J., Peters, G., Schreurs, P., and Baaijens, F., 2000, “A two-dimensional fluid structure interaction model of the aortic valve [sic],” *J. Biomech.*, **33**(9), pp. 1079–1088.
- [26] Cheng, R., Lai, Y., and Chandran, K., 2004, “Three-dimensional Fluid-Structural Interaction Simulation of Bileaflet Mechanical Heart Valve Flow Dynamics,” *Ann.Biomed. Eng.*, **32**(11), pp. 1471–1483.
- [27] Loon, R., Anderson, P., and Vosse, F., 2006, “A fluid–structure interaction method with solid-rigid contact for heart valve dynamics,” *J. Comput. Phys.*, **217**(2), pp. 806–823.
- [28] ANSYS Inc., 2013, “ANSYS User Manual.”
- [29] Païdoussis, M. P., 2014, *Fluid-Structure Interactions: Slender Structures and Axial Flow*, Academic Press.
- [30] Wall, W. A., Kuttler, U., Gerstenberger, A., Gee, M., and Forster, C., 2010, “Advances in Computational Fluid-Thin-Walled-Structure Interaction — Formulations and Solvers,” *Int. Cent. Mech. Sci.*, **519**, pp. 175–203.
- [31] *Methods and Implementation of Fluid-Structure Interaction Modeling into an Industry-Accepted Design Tool*
- [32] B. H. Menze, A. Jakab, S. Bauer, J. Kalpathy-Cramer, K. Farahani, J. Kirby, et al., "The multimodal brain tumor image segmentation benchmark (BRATS)," *IEEE transactions on medical imaging*, vol. 34, pp. 1993-2024, 2014.
- [33] S. Benzekry, C. Lamont, A. Beheshti, A. Tracz, J. M. Ebos, L. Hlatky, and P. Hahnfeldt, “Classical mathematical models for description and prediction of experimental tumor growth,” *PLoS Comput Biol*, vol. 10, no. 8, pp. e1003800, 2014
- [34] H. Murphy, H. Jaafari, and H. M. Dobrovolny, “Differences in predictions of ODE models of tumor growth: a cautionary example,” *BMC cancer*, vol. 16, no. 1, pp. 163, 2016.
- [35] A. Worschech, N. Chen, A. Y. Yong, Q. Zhang, Z. Pos, S. Weibel, V. Raab, M. Sabatino, A. Monaco, and H. Liu, “Systemic treatment of xenografts with vaccinia virus GLV-1h68

- reveals the immunologic facet of oncolytic therapy,” *BMC genomics*, vol. 10, no. 1, pp. 301, 2009.
- [36] J. Degroote, K.-J. Bathe, and J. Vierendeels, “Performance of a new partitioned procedure versus a monolithic procedure in fluid–structure interaction,” *Computers & Structures*, vol. 87, no. 11-12, pp. 793-801, 2009.
- [37] B. Muha, and S. Canić, “Existence of a weak solution to a nonlinear fluid–structure interaction problem modeling the flow of an incompressible, viscous fluid in a cylinder with deformable walls,” *Archive for rational mechanics and analysis*, vol. 207, no. 3, pp. 919-968, 2013.
- [38] S. Gholampour, “FSI simulation of CSF hydrodynamic changes in a large population of non-communicating hydrocephalus patients during treatment process with regard to their clinical symptoms,” *PloS one*, vol. 13, no. 4, 2018.
- [39] W. Bradley, “CSF flow in the brain in the context of normal pressure hydrocephalus,” *American Journal of Neuroradiology*, vol. 36, no. 5, pp. 831-838, 2015.
- [40] Takizawa K, Matsumae M, Sunohara S, Yatsushiro S, Kuroda K. Characterization of cardiac- and respiratory-driven cerebrospinal fluid motion based on asynchronous phase-contrast magnetic resonance imaging in volunteers. *Fluids and Barriers of the CNS*. 2017 Dec 1;14(1):25.
- [41] Abbey, P., Singh, P., Khandelwal, N., & Mukherjee, K. K. (2009). Shunt surgery effects on cerebrospinal fluid flow across the aqueduct of Sylvius in patients with communicating hydrocephalus. *Journal of Clinical Neuroscience*, 16(4), 514-518.
- [42] Algin, O., Hakyemez, B., & Parlak, M. (2010). The efficiency of PC- MRI in diagnosis of normal pressure hydrocephalus and prediction of shunt response. *Academic radiology*, 17(2), 181-187.
- [43] Lee, J. H., Lee, H. K., Kim, J. K., Kim, H. J., Park, J. K., & Choi, C. G. (2004). CSF flow quantification of the cerebral aqueduct in normal volunteers using phase contrast cine MR imaging. *Korean journal of radiology*, 5(2), 81-86.
- [44] Aktas G, Kollmeier JM, Joseph AA, Merboldt KD, Ludwig HC, Gärtner J, Frahm J, Dreha-Kulaczewski S. Spinal CSF flow in response to forced thoracic and abdominal respiration. *Fluids and Barriers of the CNS*. 2019 Dec 1;16(1):10.

- [45] Sweetman B, Xenos M, Zitella L, Linninger AA. Three-dimensional computational prediction of cerebrospinal fluid flow in the human brain. *Computers in biology and medicine*. 2011 Feb 1;41(2):67-75.
- [46] Maier SE, Hardy CJ, Jolesz FA. Brain and cerebrospinal fluid motion: real time quantification with M-mode MR imaging. *Radiology*. 1994 Nov;193(2):477-83.
- [47] Balédent O, Idy-peretti I. Cerebrospinal fluid dynamics and relation with blood flow: a magnetic resonance study with semiautomated cerebrospinal fluid segmentation. *Investigative radiology*. 2001 Jul 1;36(7):368-77.
- [48] Van Eijndhoven JH, Avezaat CJ, Wyper DJ. The CSF pulse pressure in relation to intracranial elastance and failure of autoregulation. In *Intracranial Pressure IV 1980* (pp. 153-158). Springer, Berlin, Heidelberg.
- [49] Beggs CB, Shepherd SJ, Cecconi P, Lagana MM. Predicting the aqueductal cerebrospinal fluid pulse: a statistical approach. *Applied Sciences*. 2019 Jan;9(10):2131.
- [50] Czosnyka Z, Kim DJ, Balédent O, Schmidt EA, Smielewski P, Czosnyka M. Mathematical Modelling of CSF Pulsatile Flow in Aqueduct Cerebri. In *Intracranial Pressure & Neuromonitoring XVI 2018* (pp. 233-236). Springer, Cham.